Carbon 222 (2024) 118924

Contents lists available at ScienceDirect

Carbon

journal homepage: www.elsevier.com/locate/carbon

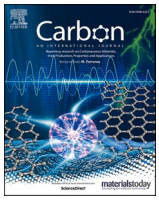

On the reduced damage tolerance of fine-grained nuclear graphite at elevated temperatures using *in situ* 4D tomographic imaging

Ming Jiang [a,b], Jon Ell [c], Harold Barnard [d], Houzheng Wu [e], Martin Kuball [f], Robert O. Ritchie [c,g], Dong Liu [a,b,*]

[a] School of Physics, University of Bristol, Bristol, BS8 1TL, UK
[b] Department of Engineering Science, University of Oxford, Oxford, OX1 3PJ, UK
[c] Department of Materials Science and Engineering, University of California, Berkeley, CA, USA
[d] Advanced Light Source, Lawrence Berkeley National Laboratory, Berkeley, CA, 94720, USA
[e] Sinosteel Advanced Materials Corporation, Zhejiang, China
[f] Center for Device Thermography and Reliability, H.H. Wills Physics Laboratory, University of Bristol, Bristol, UK
[g] Materials Sciences Division, Lawrence Berkeley National Laboratory, Berkeley, CA, 94720, USA

ARTICLE INFO

Keywords:
Fine-grained graphite
Fracture toughness
High temperatures
Raman spectroscopy
Failure strain
Fracture micro-mechanisms

ABSTRACT

Fine-grained nuclear graphite is one of the key structural materials for high temperature gas-cooled reactors as well as several Generation IV nuclear fission reactor designs. However, its deformation and fracture behaviours at elevated temperatures are not well understood. In light of this, the current study focused on investigating the flexural strength and fracture toughness of two fine-grained graphite (SNG623 and T220) using real-time X-ray computed micro-tomography imaging at room temperature, 750 °C and 1100 °C. Specifically, nonlinear-elastic fracture mechanics-based $J_R(\Delta a)$ *R*-curves at these temperatures were presented with evolution of damage and failure micro-mechanisms, local strain distributions and *J*-integral fracture analysis, purveying notable findings. Compared to the coarser-grained Gilsocarbon nuclear graphites used in the current UK Advanced Gas-cooled Reactors (AGRs), these modern fine-grained graphites display deficient fracture resistance in the form of far less stable crack growth prior to catastrophic fracture and reduced failure strain at 1100 °C. Moreover, their elevation in strength and toughness at high temperatures is remarkably lower than that of Gilsocarbon graphite. Based on *in situ* high-temperature Raman spectroscopy mapping, we believe that one of the major causes of this behaviour can be attributed to the smaller magnitude of 'frozen-in' residual stress relaxed at elevated temperatures compared with Gilsocarbon graphite.

1. Introduction

High-purity fine-grained nuclear graphite is a key material in the construction of next generation high-temperature gas-cooled reactors (HTGRs) and two Generation IV (Gen IV) reactor systems, molten salt reactors (MSRs) and very high temperature reactors (VHTRs) [1–3]. In these applications, fine-grained graphite materials have been designated to serve for various purposes including moderating and reflecting fast neutrons, physically accommodating fuel (assemblies) and control rods, providing primary circuit coolant channels for heat exchange, as well as being a load-bearing structural support comprising the majority of the core volume. In most applications, these graphite materials are not replaceable, hence limiting the lifetime of the reactors. The extreme service conditions of such nuclear reactors pose severe challenges to graphite core materials by virtue of the potentially high temperatures up to 1100 °C, fast neutron irradiation and accident conditions [4,5], all of which can significantly degrade the damage tolerance of these materials. The importance of fine-grained graphite to the structural integrity of reactor cores cannot be overstated, both from an industrial and scientific research perspective, especially for such lifetime safety critical applications.

Despite this, there has been very limited work on the fracture behaviour of these materials at elevated temperatures in particularly, for instance, there has been no high-temperature crack resistance curve published in open literature to quantify their tolerance to damage [6,7]. The lack of such understanding and quantification of the deformation

* Corresponding author. Department of Engineering Science, University of Oxford, Oxford, OX1 3PJ, UK.
E-mail addresses: Dong.Liu@bristol.ac.uk, dong.liu@eng.ox.ac.uk (D. Liu).

https://doi.org/10.1016/j.carbon.2024.118924
Received 10 May 2023; Received in revised form 16 October 2023; Accepted 9 February 2024
Available online 15 February 2024

and fracture behaviour of these fine-grained graphites reduces the confidence of knowledge transfer from past and current nuclear-grade graphite materials to fine-grained graphite for HTGRs and Gen IV reactors. As such, it has been recognised by the community that it is crucial to experimentally quantify the mechanical behaviour and damage evolution mechanisms that control the high-temperature deformation and fracture properties of these graphites to support the safe operation of advanced fission reactors [8–12]. However, such experimental characterisation is never straightforward and can be challenging as it requires real-time high-resolution imaging of the crack formation and propagation under load while the material is heated to elevated temperatures such as 1100 °C.

Nuclear graphite, in particular the coarser-grained Gilsocarbon graphite employed in the UK Advanced Gas-cooled Reactors (AGRs), is generally regarded as a quasi-brittle material with a stress-strain response consisting of an initial linear-elastic regime followed by inelastic softening and graceful failure after peak load [13–15]. It is believed that the formation, propagation and coalescence of microscopic cracks significantly give rise to graphite's global nonlinear behaviour [15–19], apart from plastic deformation by basal plane slip, cleavage and shear [20,21]. What makes it more complex is the multiple phase microstructure (filler and binder) which results in porosity ranging from nano-size to macro-scale (the total porosity volume could be as much as 20 vol.% in the as-manufactured condition) [22–24]. Despite the high preponderance of defects, as a structural material the inelastic deformation in nuclear graphite is desirable as it is a principal factor that promotes stable crack growth prior to fracture instability. Indeed, in addition to such stable cracking, multiple extrinsic toughening mechanisms – microcracking, crack deflection, crack bridging and bifurcation – have all been observed in Gilsocarbon graphite, to aid the generation of significant damage-tolerance at temperatures up to 1000 °C [25]. The large circular filler particles, distribution of cracks and pores along the path of a crack are all factors contributing to the inelasticity in Gilsocarbon graphite. In terms of fracture resistance, nonlinear elastic fracture mechanics $J_R(\Delta a)$-based crack resistance curves for Gilsocarbon graphite at 20 °C, 650 °C and 1000 °C displayed rising *R*-curves with a mean crack-initiation fracture toughness K_{Ic} values increased roughly twofold from ~ 1–1.5 MPa$\sqrt{m}$ at 20 °C to ~ 2–3 MPa$\sqrt{m}$ at 1000 °C [25]. The crack-growth toughness, represented by the steepness of the *R*-curves, also increased at the higher temperatures, as did the maximum flexural strength which was ~ 30% higher at 1000 °C than at ambient temperature. The primary factor responsible for this substantial increase in strength and toughness with increasing temperature up to 1000 °C was attributed (using high-temperature micro-Raman spectroscopy) to the relaxation of tensile residual stresses which was further evidenced by the closure of basal plane cracks in the graphite at elevated temperatures [25].

In contrast, distinctly different raw filler and binder materials are used for the synthesis of fine-grained graphite materials, with the filler cokes crushed/milled into much smaller sizes that are typically one to two orders of magnitude smaller than that in Gilsocarbon graphite [22,26–28]. This results in much smaller pore sizes, higher density and higher mechanical strength. Specifically, the macro-scale flexural strength of fine-grained graphite can be higher than 40 MPa [22,29,30] compared to flexural strengths of ~ 25–28 MPa in Gilsocarbon graphite [3,25,31,32]. Such high strength and density are deemed necessary by reactor designers to achieve a compact reactor core with intricated features to facilitate desires of higher efficiency and energy density [33,34]. However, this also brings up a negative aspect that the inelasticity of fine-grained graphite is reduced meaning its mechanical behaviour can become more brittle, potentially leading to a more catastrophic failure [2,8,22,35–37]. In fact, recent measurements on the fine-grained SNG742 and T220 graphites found their mode I fracture toughness to be 1.54 ± 0.13 MPa$\sqrt{m}$ and 1.4 ± 0.13 MPa$\sqrt{m}$ respectively [38]. Considering these values were only determined at ambient temperature with no assessment of their *R*-curve behaviour, the structural integrity of these critical nuclear materials at high service temperatures, not to mention their crack-growth toughness which defines their capacity to sustain stable cracking prior to instability, still remains unknown. It is also unclear whether the fracture-toughening mechanisms, deformation and fracture behaviour reported for Gilsocarbon graphite [25] are also applicable to these fine-grained graphites. This is a critical aspect because it determines whether the accumulated knowledge and experience of coarser-grained nuclear graphite such as Gilsoncarbon could be directly transferred to structural integrity design of reactor core components made from modern fine-grained nuclear graphite. This results in inadequate knowledge or experience on fine-grained nuclear graphite for engineers and scientists to propose new design codes, apart from adapting the ASME code and other equivalents. Consequently, it is of paramount importance that the damage-tolerant properties of fine-grained graphites are fully characterised both in terms of their macro-scale fracture toughness [39] and nano-to micro-scale mechanisms at ambient to high temperatures, to provide in-depth insight to support advanced nuclear fission system structural integrity assessment and designs.

In this study, *in situ* mechanical testing has been performed on 20 × 4 × 4 mm^3 sized specimens to measure the flexural strength and fracture toughness of two grades of fine-grained nuclear graphites, SNG623 and T220, at ambient temperature (21 °C), 750 °C and 1100 °C. Simultaneous real-time observation (hence, termed 4D) of deformation and damage process was achieved using synchrotron X-ray computed microtomography (micro-XCT) beamline at the Advanced Light Source, in conjunction with thorough digital volume correlation (DVC) analysis [40,41]. The intent of this experimental study is not only to provide an evaluation of the mechanical and damage tolerance properties of modern fine-grained graphites at service temperatures supported with mechanistic interpretation over multiple length-scales, but also to directly compare these findings with relatively well documented coarser-grained Gilsocarbon graphite [25], to demonstrate the feasibility of knowledge transfer by identifying any key concerns about reduced damage tolerance in the fine-grained graphites in the form of fracture toughness resistance and reduced failure strains. It has been found that compared to the conventional coarser-grained Gilsocarbon graphite, these two fine-grained graphite materials are stronger yet exhibit a lower increase in strength at higher temperatures. Most importantly, these materials display a significantly reduced damage tolerance compared with Gilsocarbon graphite at all temperatures. A stress-controlled failure criterion at the crack tip is considered applicable at the microscopic level. Their reduced ability to withstand damage with increasing temperature must be considered for reactor core design and safety assessment.

2. Materials and methods

2.1. Materials

The two grades of isotropic fine-grained nuclear graphite studied were SNG623 and T220 graphite, both manufactured by Sinosteel Advanced Materials Co. Ltd., China. They have been proposed as core structural materials for advanced fission reactor systems such as HTGRs and MSRs. Specifically, SNG623 graphite is moulded by isostatically pressing calcined mixture of coke filler and coal-tar pitch binder, with conventional manufacturing including re-impregnation with liquified pitch, baking and graphitisation at temperatures above 2800 °C, as reported elsewhere [42]. Details of filler coke type, source and processing route, however, have not been disclosed by the supplier, although in the as-manufactured condition, it has been reported to have an average filler grain size of ~ 20 μm, and as a result, it is classified as superfine-grained according to ASTM D7219-19 standard [43]. Its bulk density, total porosity and Young's modulus are, respectively, 1.81 g/cm^3, 17 vol.% and 11 GPa at room temperature (RT). With respect to the T220 graphite that is proposed for MSRs to prevent molten salt infiltration and gaseous

product permeation, benefiting from their finer porosity at millimetre and micrometre scales, there is very limited open literature on its as-manufactured properties or the raw materials used, but it is known to be isostatically moulded with an average filler grain size of ~ 5 μm; hence, it is classified as ultrafine-grained with a bulk density of 1.87 g/cm^3 and a Young's modulus of 11 GPa at RT [44]. The compressive strength of T220 is reported to be 120 MPa which is higher than the compressive strength of 93 MPa in SNG623. The total porosity in T220 is not well-documented with ~ 3.0–5.5% reported based on a 2D optical image analysis only, which we believe is not representative for the bulk porosity population [44].

2.2. Mechanical testing

Measurement of the flexural strength of T220 and SNG623 was performed using unnotched rectangular graphite beams tested in three-point bending. Corresponding fracture toughness testing involved single-edge notched bend SE(B) rectangular beam specimens also in three-point bending; further details are given in Supplementary Material, Section 1. Specifically, all unnotched and notched beam specimens had identical dimensions of 20(L) × 4(W) × 4(B) mm and were prepared by electrical discharge machining. The beams for fracture toughness testing contained a notch of a_o ~1.8 mm long, representing an a/W ratio of 0.45, where W is the width of the beam. Starting notches were prepared by using a diamond saw to cut a starter notch, 1.2 mm in length and 400 μm in width, followed by a micro-notching technique for fine polishing the notch root by using a razor blade immersed 1 μm diamond paste; this gave a sharp notch root radius of ~ 30 μm.

Both types of mechanical tests were conducted in a dedicated high-temperature hot cell integrated with a three-point bending fixture in inert Ar gas environment at the X-ray computed micro-tomography (micro-XCT) beamline BL 8.3.2 of the Advanced Light Source (ALS, Lawrence Berkeley National Laboratory, Berkeley, USA). This experimental setup allows for synchrotron micro-XCT to image in real time the deforming materials in the hot cell chamber in 3D while the loading is being applied under elevated temperatures up to 1100 °C, *i.e.*, *in situ* 4D imaging of damage evolution and crack initiation and propagation. Detailed descriptions of this beamline hot cell and the experimental set up are described elsewhere [25,41,45–48]. A monotonically increasing load was applied to all specimens under displacement-control at a displacement rate of 1 μm s^{-1}. All specimens were first scanned by micro-XCT under a load-free condition for reference.

For flexural strength measurements, eight T220 unnotched beam specimens were tested: four at room temperature, two at 750 °C, and two at 1100 °C. Seven corresponding SNG623 specimens were tested: three at RT, two at 750 °C, and two at 1100 °C. Three to four micro-XCT scans were performed for each of these unnotched specimens starting from load-free condition to 82–92% of failure load except for one T220 specimens in which a final scan was only taken at 66% of its final failure load.

For fracture toughness measurements, seven T220 SE(B) specimens were tested: three at RT, two at 750 °C, and two at 1100 °C; seven corresponding SNG623 SENB specimens were tested: two at RT, two at 750 °C, and three at 1100 °C. Four to eight scans were performed starting from the load-free condition up to over 92% of the failure load where the specimens fractured unstably after slow crack growth. The initiation and propagation of cracks were successfully imaged and crack lengths were measured by uniformly sampling across specimen thickness giving an average value with standard deviation from more than 10 values at each loading step.

2.3. Synchrotron X-ray computed micro-tomography (micro-XCT)

Synchrotron micro-XCT scans were carried at beamline 8.3.2 of the Advanced Light Source, Berkeley, USA. A beam energy of 25 keV was used with a voxel size of 3.25 × 3.25 × 3.25 μm^3 and field of view ~ 8 × 4 mm. A set of calibration scans using a bright- and dark-field image were taken prior to each actual scan for the purpose of determining appropriate sample position and for correcting X-ray intensities (stray light removal). A total number of 1969 projections were acquired for each scan which were reconstructed to micro-XCT images using a dedicated filtered back-projection algorithm in the software programme Octopus 8.5 [49] at beamline 8.3.2, ALS.

2.4. Raman spectroscopy measurement

It has been widely recognised that mechanical machining including cutting, grinding and polishing can introduce additional damage to the surface of graphite, therefore the crystal properties at elevated temperatures are best measured on freshly fractured surfaces to exclude the effect of sample preparation [22,50]. A Renishaw inVia Raman Microscope (Renishaw plc, UK) equipped with a Linkam TS1500 high-temperature stage (Linkam Scientific Instruments Ltd., UK) was employed for high-temperature Raman mapping to evaluate residual stresses. Specifically, a 488 nm blue laser (Ar^+ excitation energy 2.54 eV, Coherent Sapphire 488-50 SF NX model) with nominal output power of 4 mW (10% of 40 mW output power) was used for exciting the Raman spectra. The laser was focused on the graphite fracture surfaces using a × 50 Nikon TU PLAN ELWD long working distance (11 mm) objective lens with a numerical aperture (NA) of 0.6 (a long working distance is used to avoid touching and hence damaging the objective lens with high-temperature stage shielding glass during focusing). This gives a laser focal spot size on the graphite surface of ~ 1–2 μm [25,51]. Two randomly selected regions of interest (ROIs) were mapped on the T220 and SNG623 graphite fracture surfaces from RT up to 800 °C in five temperature steps, *i.e.*, at RT, 100 °C, 350 °C, 450 °C, 800 °C; this was performed in an inert environment of argon gas (99.998% Pureshield Argon Cylinder Industrial Grade, BOC Ltd., UK). One of the ROIs was mapped using a square grid of 11 × 11 points with grid step size of 4 μm (mapping area 40 × 40 μm^2), the other by a square grid of 11 × 11 points with grid step size of 3 μm (mapping area 30 × 30 μm^2). Twenty maps were carried out in total – one mapping location at each temperature for each material, giving 4 × 5 × 121 = 2420 spectra in total. The setup is also listed in Table 1.

Each Raman spectrum was collected in a Raman shift range of 100–3200 cm^{-1} with an exposure time of 10 s with one accumulation per spectrum acquisition using a 3000 lines/mm visible grating and a Renishaw Centrus 05TJ54 detector. Prior to each Raman mapping procedure, the spectrometer was calibrated using a single crystal Silicon wafer peaking at 520.3 cm^{-1} by 4 mW laser power. Collected Raman spectra were fitted with the Renishaw's proprietary WiRE 5.3 software system using a Voigt profile (mixed Gaussian + Lorentzian) based on a

Table 1
Summary of high temperature Raman mapping setups. Two randomly selected regions of interest (ROIs, also called locations) are mapped from both T220 and SNG623 graphite's freshly fractured surface (FFS) individually from room temperature (21 °C) up to 800 °C.

	Specimen NO.	Location NO.	Temperature (°C)	Grid resolution	Step size (μm)
T220	1	1	RT→100 → 350→450 → 800	11 × 11 square grid	4
		2	RT→100 → 350→450 → 800	11 × 11 square grid	3
SNG623	1	1	RT→100 → 350→450 → 800	11 × 11 square grid	4
		2	RT→100 → 350→450 → 800	11 × 11 square grid	3

least-square approach with fitting tolerance of 0.00001 and maximum iteration number of 2000. Cosmic ray and background removal based on a linear baseline were additionally performed. As previous experience on coarser-grained GCMB grade Gilsocarbon graphite had indicated a hydrostatic stress conversion factor of ~180 ± 5 MPa per cm^{-1} shift in G-band position [25], this stress conversion factor was directly applied to the T220 and SNG623 graphite in the estimation of residual stresses at both ambient and high temperatures. More details are given in Supplementary Material, Section 4.

2.5. Data analysis

Reconstructed micro-XCT data were processed in an open-source image processing package FiJi-ImageJ [52,53] (Original ImageJ: National Institutes of Health, USA, https://imagej.net/software/fiji/) for 16-bit to 8-bit TIFF image format conversion, brightness and contrast adjustment and noise filtering. For both the unnotched and SE(B) specimens scanned, datasets were cropped to identical dimensions individually for digital volume correlation (DVC) analysis in a commercial scientific data analysis software Avizo Standard 2021.2 (Avizo, Thermo Fisher Scientific, USA). DVC was carried out following a multi-pass procedure [40,54,55] such that the interrogation window size (subset size) was iterated from 96 × 96 × 96 to 64 × 64 × 64 and eventually to a 32 × 32 × 32 voxels [3] for correlating the dataset from the first deformed step to the initial load-free step; each of the latter two utilised the displacement field computed from its previous pass, for the purpose of improving correlation quality and therefore accuracy in computed displacements and strain fields. This was followed by correlating each tomographic dataset at each subsequent loading step to its preceding loading step at 32 × 32 × 32 voxels [3]. Displacement and strain fields ahead of the crack tip in the fracture toughness specimens were taken at crack initiation to enable nonlinear-elastic fracture mechanics based *J*-integral calculations in a dedicated JMAN code [56] to evaluate the mode I fracture toughness K_{Ic} under plane-strain condition using Young's modulus of 12 GPa (to account for 10% modulus increase at high temperature [57]), a Poisson's ratio of 0.2 and a yield strength of 20 MPa. More details of DVC methodologies and brief descriptions of JMAN procedure are in given in Supplementary Material, Section 2 and 3. Full details of the JMAN code are described elsewhere [56].

Values of the flexural strength, σ_f, in three-point bending were determined from:

$$\sigma_f = \frac{3PL}{2BW^2}, \tag{1}$$

where P is the applied load force, L is the loading span of 16 mm, B is the specimen thickness of 4 mm and W is the specimen width of 4 mm, for all the unnotched specimens tested. The corresponding flexural modulus E was calculated from:

$$E = \frac{mL^3}{4BW^3}, \tag{2}$$

where m is the initial linearity constant of the load-displacement curve. Representative load-displacement curves can be found in the Supplementary Materials Section 1. Estimated flexural moduli were found to increase with temperature for the two grades of graphite which have also been included the Supplementary Materials Section 1. The strain at the tensile surface of beam mid-span computed by DVC was compared with beam bending theory for two room temperature specimens with the difference being found to be small (~ 5%). These can also be found in the Supplementary Materials Section 2. It is suggested that reliable measurements of modulus need to be obtained from standard flexure or uniaxial tension/compression tests with the strains measured and stress derived from suitable beam theory. In the present work, the flexural modulus calculation is for reference only due to both the short beam length (length to width ratio $L/W = 5$ in our case) and the quasi-brittle and porous nature of nuclear graphite.

The fracture toughness was calculated as the critical value of the *J*-integral at crack initiation and during subsequent stable crack growth. This was achieved using nonlinear elastic fracture mechanics methodologies in general accordance with ASTM Standard E1820 to determine the elastic ($J_{el(i)}$) and inelastic ($J_{pl(i)}$) contributions to the measured *J*-integral (J_i), *viz.*:

$$J_i = J_{el(i)} + J_{pl(i)} = \frac{K_i^2}{E'} + J_{pl(i)}, \tag{3}$$

where $E' = E/(1- \nu^2)$ for plane-strain condition, E is Young's modulus, ν is Poisson's ratio, and K_i is the linear-elastic stress intensity factor at each data point on the measured load-displacement curve which is calculated by:

$$K_i = \left[\frac{P_i L}{(BB_N)^{0.5} W^{1.5}}\right] f\left(\frac{a_i}{W}\right), \tag{4}$$

where B_N is the net specimen thickness, $B_N = B$ when no side grooves are used. P_i is the applied load at each individual data point and $f(a_i/W)$ is a geometry-dependent function of the ratio of crack length, a_i, to width, W, as listed in the ASTM E1820 standard for single-edge notched three-point bending specimen geometry:

$$f\left(\frac{a_i}{W}\right) = \frac{3\left(\frac{a_i}{W}\right)^{0.5}\left[1.99 - \left(\frac{a_i}{W}\right)\left(1 - \frac{a_i}{W}\right)\left(2.15 - 3.93\left(\frac{a_i}{W}\right) + 2.7\left(\frac{a_i}{W}\right)^2\right)\right]}{2\left(1 + 2\left(\frac{a_i}{W}\right)\right)\left(1 - \left(\frac{a_i}{W}\right)\right)^{1.5}}, \tag{5}$$

In this present work, crack length a_i was obtained by averaging more than 12 crack length values uniformly sampled across specimen's thickness from each micro-XCT scanned load step P_i. The inelastic contribution to J, $J_{pl(i)}$, was defined as:

$$J_{pl(i)} = \frac{1.9A_{pl}}{B_N b_i}, \tag{6}$$

where b_i is the residual ligament at a specific crack length a_i such that $b_i = W - a_i$. A_{pl} is the area under the force load-line displacement curve accounting for the inelastic deformation. Using this approach, the value of J_i can be determined at any point along the force load-line displacement curve. Together with the corresponding crack lengths a_i, the J-Δa resistance curve can thus be determined with Δa being the difference of the individual a_i during testing and the initial crack length a_0 after precracking. The mode I fracture toughness K_{IC} expressed in terms of the stress intensity was then back calculated using the standard mode I J-K equivalence relationship $K_{IC} = (J_{IC}E')^{0.5}$, and $E' = E/(1- \nu^2)$ for plane-strain condition.

3. Results

3.1. Strength and $J_R(\Delta a)$ resistance curve at elevated temperatures

As noted above, two fine-grained nuclear graphites, namely SNG623 and T220, were examined in this study; details on these materials are described in Materials and methods section. The flexural strength, and fracture toughness in the form of $J_R(\Delta a)$ *R*-curves of SNG623 and T220 at 21 °C, 750 °C and 1100 °C are presented in Fig. 1. Both fine-grained graphites demonstrate a small increase in flexural strength with increase in temperature from 21 °C to 1100 °C. Specifically, SNG623 shows a 12% increase from ~ 55 MPa at 21 °C to ~ 62 MPa at 1100 °C, whereas T220 shows a 10% increase rising from ~ 48 MPa at 21 °C to ~ 53 MPa at 1100 °C. Neither of these increases is as significant as the ~ 30% improvement exhibited by Giloscarbon graphite from 21 °C to 1000 °C [25], although the fine-grained graphites have flexural strength some 2 to 3 times higher than Gilsocarbon grapihte.

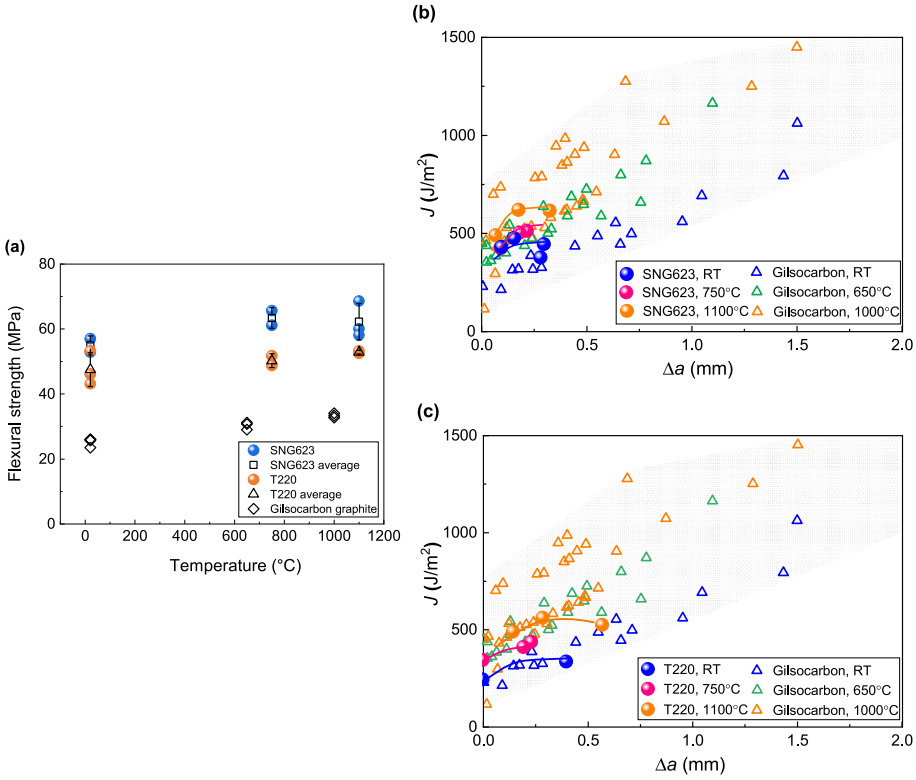

Fig. 1. Flexural strength and $J_R(\Delta a)$ *R*-curve of the SNG623 and T220 fine-grained graphite at 21°C, 750°C and 1100°C. (a) Measured flexural strengths of SNG623 and T220 graphite materials as a function of temperature. SNG623 has slightly higher flexural strength than T220 but both materials show a 10–12% higher strength at 1100 °C compared to that at room temperature. By comparison, coarser-grained Gilsocarbon graphite in the previous work [25] displays a ~ 30% increase in flexural strength at 1000 °C, but its overall strength is markedly lower than that of SNG623 and T220. Nonlinear-elastic fracture mechanics-based $J_R(\Delta a)$ *R*-curves for (b) SNG623 and (c) T220 graphites at ambient to elevated temperatures again compared to Gilsocarbon graphite. The fine-grained graphites exhibit a much smaller increase in toughness with increasing temperature compared to that in Gilsocarbon. The difference in toughness between these fine-grained graphites and Gilsocarbon is most acute in the crack-growth regime where the extent of stable crack extension prior to instability in SNG623 and T220 is almost negligible in comparison to the extensive stable crack extension in the coarser-grained Gilsocarbon graphite. Data for Gilsocarbon graphite are reproduced from Ref. [25].

In situ 4D observation (with the 4th dimension being time) and quantification of crack extension in the form of nonlinear-elastic fracture mechanics-based $J_R(\Delta a)$ *R*-curve measurements were used to measure the fracture toughness where crack-tip energy release rate *J* is plotted as a function of crack extension Δa (Fig. 1). Crack-initiation K_{Ic} toughness, back-calculated from the critical *J* values, revealed a ~ 30% increase in toughness with increasing temperature: from ~ 1.6–1.9 MPa$\sqrt{m}$ at 21 °C to ~ 2.3 MPa$\sqrt{m}$ at 1100 °C for SNG623, and from ~ 1.4–1.6 MPa$\sqrt{m}$ at 21 °C to ~ 1.9–2.0 MPa$\sqrt{m}$ at 1100 °C for T220. These toughness values are comparable but slightly lower than that measured for Gilsocarbon at 1100 °C. What is distinctly different in the fine-grained graphites is the very limited extent of their *R*-curves. Both SNG623 and T220 display minimal stable crack extension Δa at all temperatures prior to final fracture: 0.3 mm for SNG623 and 0.5–0.6 mm for T220 compared to ~ 1.2 mm for Gilsocarbon. The reasons underlying this reduced damage tolerance in fine-grained graphites are outlined in the following sections by analysing their toughening mechanisms and relaxation of residual stresses at elevated temperatures.

3.2. *Toughening mechanisms for crack initiation and growth*

X-ray computed micro-tomography (μXCT) images showing the fully developed crack profiles at failure load in SNG623 and T220 graphite at 21 °C, 750 °C and 1100 °C are given in Fig. 2a. These images are extracted from the central volumes of the μXCT captured region where the main crack is contained, as in Fig. 2b. Crack paths at final fracture for both two grades of graphite at 21 °C, 750 °C and 1100 °C are in general relatively straight and in Mode I, *i.e.*, nominally perpendicular to tensile crack-opening direction (shown by the white arrows). Two example 3D renderings of the fully developed crack face at 1100 °C are given in Fig. 2c, demonstrating the relatively straight crack profile without much tortuosity and bifurcation extended throughout the entire bulk volume. As Gilsocarbon graphite demonstrated significantly improved damage-tolerance at elevated temperatures, in the form of steeper *R*-curves with ample evidence of extrinsic toughening from crack deflection and crack bridging [25], we therefore conducted a comprehensive examination of tomographic images of the deformation and fracture of these fine-grained graphites (Fig. 3) to seek evidence contributing to their more limited crack-growth resistance at elevated temperatures.

Of importance here is that in the fine-grained graphites there are essentially no characteristic filler particles that are found in abundance in the coarser-grained Gilsocarbon graphite; this is due to the fact that the filler cokes are grounded or milled into micrometre-sized grains as starting materials. The dense regions with high greyscale values in Fig. 3 are in fact clusters of grounded filler particles with less porosity compared with the binder areas; these are referred to as “filler particle regions” and labelled as “F” in Fig. 3c). Round and irregularly shaped pores in the binder regions are uniformly distributed. No distinctive boundary between filler region and binder matrix can be seen. In these SNG623 and T220 graphites, there are predominantly three types of mechanisms where an incipient crack interacts with these characteristic microstructural features to generate extrinsic toughening: uncracked ligament bridging, crack bifurcation and crack deflection, as shown in Fig. 3. Interestingly, evidence of extensive microcracking is not apparent.

Uncracked-ligament bridging (Fig. 3a): this form of crack bridging, which is quite common in brittle solids, results from uncracked regions in the wake of the main crack tip; these bridges then carry load that

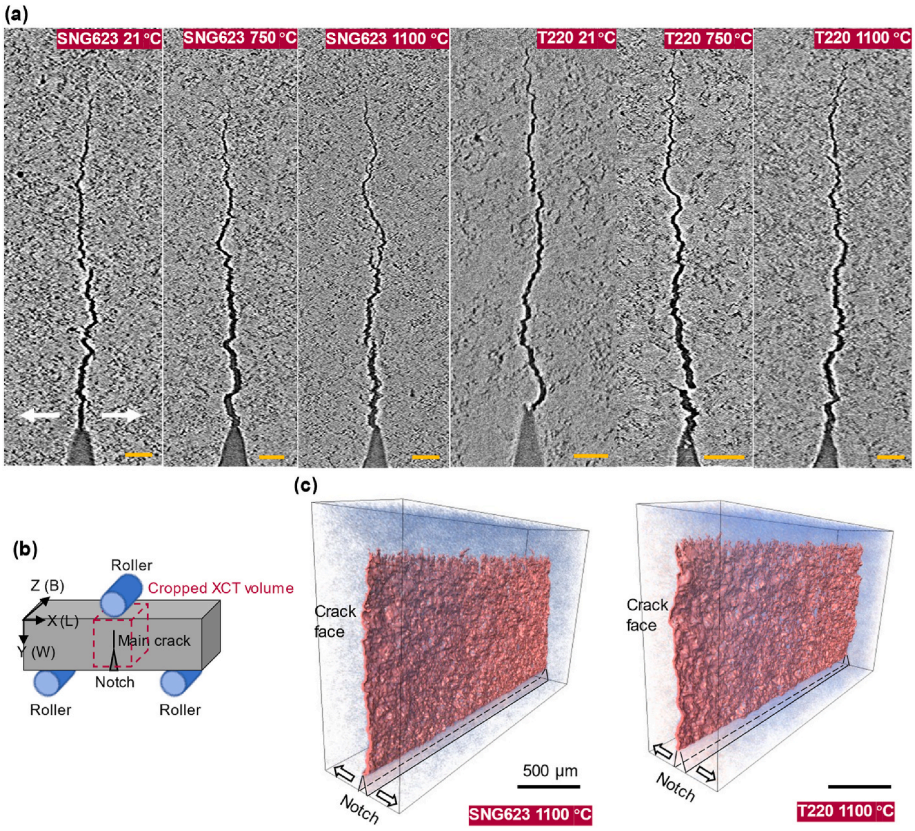

Fig. 2. X-ray computed micro-tomography (µXCT) images showing the fully developed crack profiles in SNG623 and T220 graphite at 21°C, 750°C and 1100°C. (a) Crack paths at final fracture for both SNG623 and T220 fine-grained graphites at 21 °C, 750 °C and 1100 °C are in general relatively straight and in Mode I, *i.e.*, nominally perpendicular to tensile crack-opening direction (shown by the white arrows). (b): Schematic showing the location of 3D reconstructed volumes in (c) relative to the specimen. (c): Two example 3D renderings of the fully developed cracks in SNG623 and T220 graphite at 1100 °C. Closer inspection revealed various forms of extrinsic toughening mechanisms that are shown in Fig. 3. All scale bars 100 µm unless stated otherwise. False colours are for visual guidance only. More examples of fully developed cracks can be found in Supplementary Materials for both 21 °C and 1100 °C.

would otherwise be used to propagate the fracture. It is observed in both SNG623 and T220 graphite at all temperatures where short segments of the crack remain unconnected at considerable distances behind the main crack tip, including cracks formed nominally parallel to the main crack (Fig. 2 and Fig. 3a). These intact bridging events are mostly associated with the neighbouring regions around clusters of filler grains (dense regions, F in Fig. 3c). However, there is little evidence that the frequency of the bridging sites changes with increase in temperature.

Crack bifurcation (Fig. 3b): the bifurcation of cracks is clearly seen in the fine-grained graphites at all temperatures, and is depicted by shorter crack segments stemming from a main crack and growing in a different direction to that of the main crack, as shown in Fig. 3b. These branched secondary cracks are mostly created when the main propagating main crack connects with fine porosity in the vicinity of the crack tip; the resulting bifurcated crack segments are generally shorter than 100 µm.

Crack deflection (Fig. 3c): deviations of the main crack path out of the Mode I plane are predominantly seen in the fine-grained graphites when the main crack encounters a stiffer and denser region such as filler regions. Frequently, the crack will penetrate through these regions via pores or weakly bonded filler-binder/filler-filler regions, leading to local 'zig-zag' crack trajectories in a number of instances where the crack deflection angle is as large as 90°, *i.e.*, parallel to crack opening direction, as in Fig. 3c). However, the degree of crack deflection and the tortuosity of the crack paths is far less than that observed in the coarser-grained Gilsocarbon graphite, due to the relatively small sizes of the filler particles in the fine-grained graphites. However, a rigorous quantification of the number and extent of these extrinsic toughening mechanisms especially in 3D at different temperatures is still lacking, and more advanced image detection algorithms with 3D extension or deep learning based approach could potentially offer a quantitative way for examining the total population of toughening mechanisms.

These crack morphological features and resulting extrinsic toughening mechanisms are seen in the fine-grained graphites at all temperatures between 21 °C and 1100 °C. Further, some of the fractures did not initiate at the notch, but rather at a certain location ahead of the notch root (Supplementary Material, Section 7). This is typical of brittle materials that fail under a local stress-controlled fracture criteria, demonstrating the competition between the local tensile stresses (which peak close to, yet ahead, of the notch within two crack-opening displacements of the root) and the statistical probability of finding the weakest defects (which increases with distance ahead of the notch). However, unlike Gilsocarbon [17], there was no substantial inelasticity from microcracking at low and high temperatures or more evidence of toughening from any mechanism in SNG623 and T220 graphite at elevated temperatures, including a change in the global stress-strain linearity. This is evidenced by the strain behaviour derived from the digital volume correlation (DVC) analysis in the following section.

3.3. 3D strain distribution in unnotched and notched configuration

To further understand the load bearing capability and 3D strain development in these fine-grained graphite materials, we conducted a comprehensive DVC analysis on the micro-XCT datasets collected at increasing load steps. To start with, a thorough DVC sensitivity study was performed to evaluate the resolution, uncertainties and the cross-correlation coefficient to increase the confidence of the analysis. The

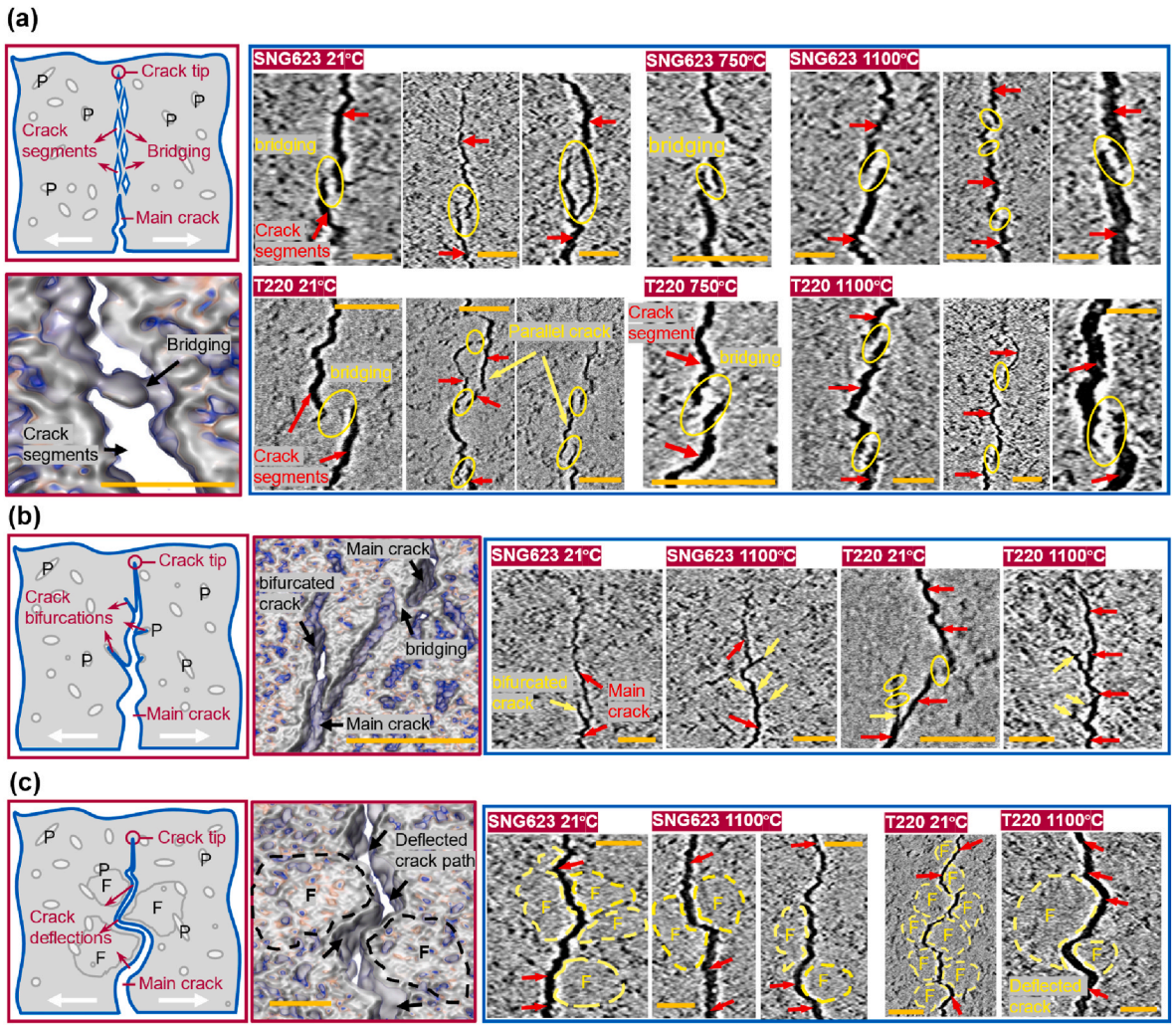

Fig. 3. Various forms of extrinsic toughening and crack shielding mechanisms are present. (a) Exaggerated schematics and a 3D rendering of uncracked-ligament bridging (crack bridging). Label P: simplified schematic of pores. Typical examples of crack bridging in both SNG623 and T220 graphite at 21 °C, 750 °C and 1100 °C are shown. Yellow circles: bridging sites of ligaments; Red arrows: crack segments. Parallel cracks can also be seen and are labelled. (b) Schematic and 3D rendering showing crack bifurcation and branching, with examples shown for both SNG623 and T220 graphite at 21 °C and 1100 °C. (c): Schematic and 3D rendering showing crack deflection, with examples also shown for both SNG623 and T220 graphite at 21 °C and 1100 °C. Propagating cracks are often deflected by dense filler regions (labelled as F, encircled in yellow dashed lines) such that the crack tunnels through these regions via weak sections that are often associated with porosity between the filler regions and between the filler and binder. Both branched and bifurcated cracks are in general shorter than 100 μm. All scale bars: 100 μm. All schematics not drawn to scale. Other examples of the corresponding behaviour at 750 °C can be found in Supplementary Material, Section 5.

strain uncertainty has been determined to be 100 με in our study; full details are given in Supplementary Material, Section 2. Full field displacement and strain are computed within a volume of ~ 7 mm (length, L) × 3.7 mm (in-plane width, W) × 3.7 mm (out-of-plane thickness, B) for the unnotched beams and ~ 4.7 mm (L) × 2.5 mm (W) × 3.5 mm (B) for notched beams based on the cross-correlation between reference and deformed datasets. This enabled a 3D strain quantification with micrometre-scale resolution for flexural strength tests and a direct observation and quantification of the displacement and strain development with crack initiation and growth chronologically, *i.e.*, 4D imaging, in fracture toughness tests.

For the bending of the unnotched beams, strain distribution for the SNG623 graphite was derived at 92% of the failure load (P_f) at 21 °C, and at 82% of the failure load (P_f) at 1100 °C. The strain distribution at these two loading steps on the tensile surface of the beam (marked by dashed square in Fig. 4a) were extracted and plotted as a histogram in Fig. 4b. Similar procedures were used for the T220 specimens at 66% P_f (at 21 °C) and 92% P_f (at 1100 °C), also as in Fig. 4(a-b). It can be seen that at the high temperature of 1100 °C, the magnitude of the strains in T220 graphite is in general 30% lower than that at 21 °C.

As expected from a three-point bending configuration, the highest tensile strains were distributed at the central region of the bottom tensile surface where ultimate failure ensued. Therefore, strain values from this central region of the specimens, ~ 2 mm (L) × 3.7 mm (W) × 3.7 mm (B) as in Fig. 4a, were extracted and averaged. For the SNG623 graphite, the averaged strain on the tensile surface at 92% P_f was 4600 ± 280 με (at 21 °C), and 3640 ± 210 με at 82% P_f (at 1100 °C), as shown in Fig. 4(b-c). For the T220 graphite, the tensile strains at 66% P_f (at 21 °C) were 2850 ± 120 με, and 2790 ± 340 με at 92% P_f (at 1100 °C).

Linearly extrapolating these tensile surface strains to 100% P_f gives ~ 5000 ± 100 με for the failure at 21 °C and 4430 ± 100 με at 1100 °C for SNG623, and 4330 ± 100 με at 21 °C and 3030 ± 100 με at 1100 °C for T220; the uncertainty in these strains from DVC was estimated to be 100 με, as described in Supplementary Material, Section 2. The key messages from these results are: (i) the tensile failure strains developed in the SNG623 graphite at both room and high temperatures are higher than in the T220 material, and (ii) the tensile failure strains at 1100 °C are somewhat surprisingly lower than those developed at 21 °C for both

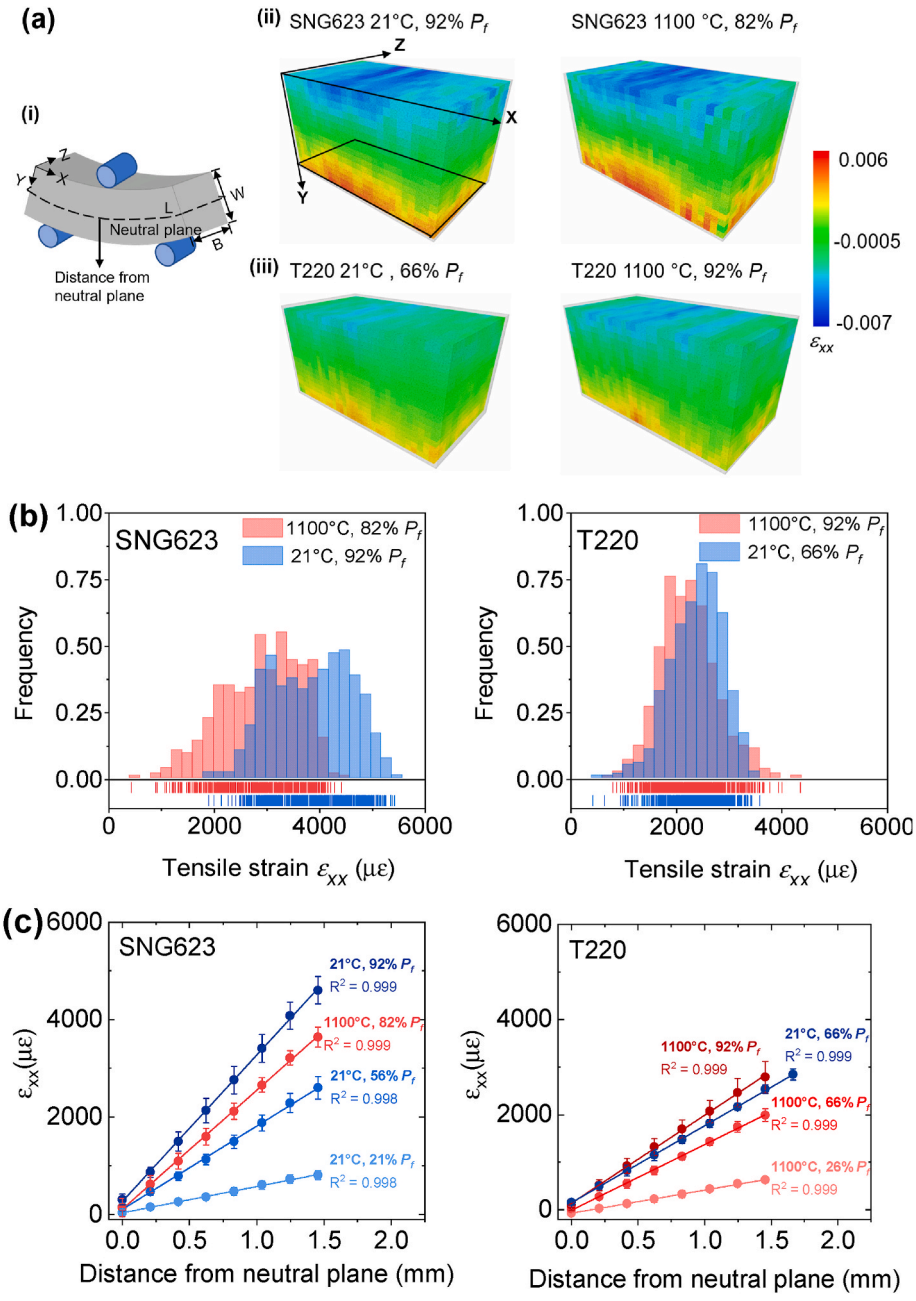

Fig. 4. Digital volume correlation (DVC) of unnotched beam specimens for quantifying 3D full field displacement and strain in flexural strength test. (a) DVC computed strain field in unnotched SNG623 and T220 graphite beams tested at 21 °C and 1100 °C. Exaggerated schematic in (i) depicts 3-point bending configuration and coordinates defined. (b) Histograms of tensile strain ε_{xx} at beam tensile surface, as the dashed box plane in (a). Tensile ε_{xx} strains in SNG623 are in general higher than in T220 graphite. Tensile ε_{xx} strain in T220 graphite when loaded to 92% failure load (P_f) at 1100 °C is in a similar range to that when only loaded to 66% P_f at 21 °C. (c) Linear distribution of tensile ε_{xx} strains across beam width W plotted as a function of distance from neutral plane. SNG623 and T220 graphites exhibit no nonlinear increase of tensile strains up to ~1.5 mm from neutral plane at both 21 °C and 1100 °C. T220 graphite failure strain at 1100 °C is ~30% lower than at 21 °C.

grades of graphite. In addition, the tensile ε_{xx} strains, extracted and averaged from beam centre ~ 2 mm (L) × 3.7 mm (W) × 3.7 mm (B) is plotted in Fig. 4c across the beam width (W) as a function of the distance from bending beam's neutral plane at different loading steps. The corresponding tensile ε_{xx} strains in SNG623 graphite at 21 °C linearly increase with increasing distance away from neutral axis, again showing no trace of nonlinearity even at 92% P_f (at a distance of 1.5 mm a strain of 4600 ± 280 με was formed). The same trends can be seen for SNG623 tested at 1100 °C (at 82% P_f). The T220 graphite at 1100 °C exhibits a similar linearity in the distribution of the tensile ε_{xx} strains (at 92% P_f) with increasing distance from neutral axis. Such linear increase of tensile strain ε_{xx} with distance from neutral plane has also been testified by averaging the ε_{xx} across another two different mid-span lengths ($L = 1.2$ mm and $L = 0.6$ mm) and it is considered to be valid for all these three cases, providing solid evidence substantiating our arguments. These can be found in Supplementary Materials.

These observations for both fine-grained graphites are distinctly different to the previous findings on the coarser-grained Gilsocarbon graphite where the bulk tensile strains plateaued at a strain of ~ 1500 με at room temperature and ~ 2500 με at 1000 °C at 90% P_f, essentially at the same location [25], under the same testing method and specimen geometry. Further, the shearing effect from short beam three-point

bending has been examined by plotting distributions of shear strain components ε_{xy}, ε_{xz} and ε_{yz} (schematics see Fig. 4a) from the highest loading step computed by DVC in both SNG623 and T220 graphite at both RT and 1100 °C. The shear strain ε_{xy} has a bimodal distribution with a largest magnitude of about 1000 με in general. The distribution peaks for these bimodal distributions are all located at the magnitude of about 500 με in all cases. This means that the shear strain component ε_{xy} is mostly less than 10% of the maximum tensile strain (ε_{xx}). The distribution for the other two shear strain components, ε_{xz} and ε_{yz}, are having rather symmetric distribution around zero strain. The magnitude for ε_{xz} and ε_{yz} is in general smaller than 500 με in all cases. Detailed distributions of these shear strains can be found in Supplementary Materials.

Full-field 3D displacement and strain were also computed by DVC for notched beams employed for the fracture toughness testing (Fig. 5). The displacement fields ahead of the crack tip was used to derive local *J*-integral analysis using the J-MAN code originated from Becker et al. [56]; the details of analysis are included in the Materials and Methods section and in Supplementary Material, Section 3. Such *J*-integral analysis involved a conventional finite element analysis procedure in which a linear elastic material property model and stress-strain relationship was implemented in this study. Specifically, six to eight path-independent *J*-integrals from different contours were evaluated ahead of the crack tip, and the critical value of *J* determined at the onset of crack initiation (shortest crack that was captured by micro-XCT imaging), J_{Ic}. The mode I linear-elastic fracture toughness value K_{Ic} (sometimes referred to as K_{JIc}), was back-calculated based on mode I *J*-*K* equivalence under plane-strain assumption (Fig. 5c). The calculated crack initiation *J*-integral values and K_{Ic} from all contours converge to a

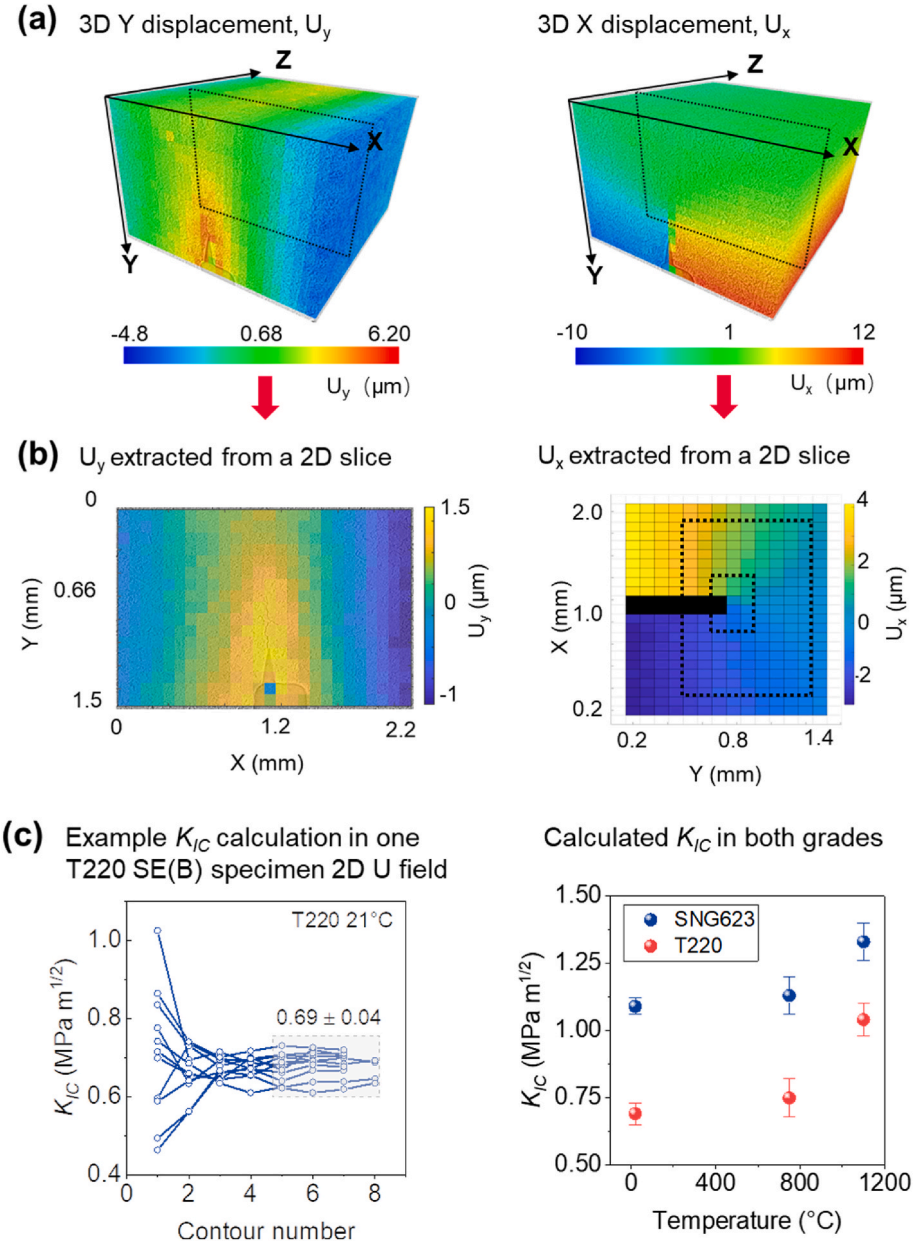

Fig. 5. DVC computed 3D displacement field in a SE(B) T220 beam at 21°C and example of *J*-integral and K_{Ic} evaluation by using JMAN numerical approach [56]. (a) 3D Y and X displacement, U_y and U_x at a crack length of 0.42 ± 0.07 mm in a SE(B) T220 beam at 21 °C, as an example. (b) 2D planes (dashed lines in (a)) of such 3D displacement fields are extracted across SE(B) beam middle Z ~ 1–1.5 mm to be used for *J*-integral and K_{Ic} evaluation at crack initiation by numerical JMAN approach. Dashed box in bottom right figure exemplifies the inner and outer contour for area integral. (c) 6 to 8 contours are calculated for each set of 2D U_y and U_x displacements. Results are plotted for all 2D planes across Z direction, showing K_{Ic} values stabilise after the 5th contour. Mean ± standard deviation of converged K_{Ic} values reported for each specimen are plotted against temperatures, showing a slight increase in fracture toughness with temperature.

stable value to produce an average ± standard deviation of six to ten sets of 2D displacement fields, Fig. 5c. The calculated crack-initiation K_{Ic} toughness values for SNG623 graphite at 21 °C, 750 °C and 1100 °C were 1.09 ± 0.03 (crack length 0.19 ± 0.05 mm), 1.14 ± 0.07 (crack length 0.25 ± 0.04 mm) and 1.33 ± 0.07 MPa$\sqrt{m}$ (crack length 0.17 ± 0.03 mm), respectively; the corresponding values for T220 at 21 °C, 750 °C and 1100 °C are 0.69 ± 0.04 (crack length 0.42 ± 0.07 mm), 0.75 ± 0.07 (crack length 0.30 ± 0.06 mm) and 1.04 ± 0.06 MPa$\sqrt{m}$ (crack length 0.31 ± 0.06 mm) respectively (Fig. 5c). These values are close to those described above based on calculations made using ASTM E1820 Standard [58]. A limited rise in fracture toughness with increasing temperature can be seen.

3.4. Residual stresses at elevated temperatures

A previous study [25] on the coarser-grained Gilsocarbon graphite with the same specimen geometry and testing method revealed a significant relaxation in tensile residual stresses due to closure of nano-scale thermal shrinkage cracks at elevated temperatures, which was deemed to provide a major contribution to the measured increase of strength and fracture toughness at 1000 °C evidenced from high temperature micro-Raman spectroscopy mapping. Similarly, a 20% increase in disc splitting tensile strength has been reported in Gilsocarbon graphite tested at 850 °C with similar reason being attributed to one of the mechanisms that gives Gilsocarbon graphite higher resistance to microcracking and tensile failure [59]. However, as described above, for both SNG623 and T220 fine-grained graphites, the increase in strength and toughness at high temperature is far less pronounced. To investigate this, *in situ* high-temperature Raman mapping with micrometre-scale resolution was conducted on the fine-grained graphites over a range of temperatures between 21 °C and 800 °C.

Two regions of interest (40 × 40 μm^2 and 30 × 30 μm^2) were randomly selected from each material (SNG623 and T220) on freshly fractured surfaces (to rule out additional stresses caused by any mechanical machining [22,50]) with one Raman map taken for each region at 21 °C, 100 °C, 350 °C, 450 °C and 800 °C. Each map involved 121 spectra and for each sample, 1210 spectra were analysed for each graphite, as described in the Materials and methods section. As is well known with in spectroscopy and diffraction methods, the reference stress-free shift is difficult to determine, in the present work, the 'variation' of stresses within a mapped area was used. Example Raman spectra of these two grades of fine-graiend graphite at elevated temperatures are given in Fig. 6, showing characteristic nuclear graphite Raman bands (D-, D′-, G- and G′-bands etc.) and band position shift due to high temperature induced phonon frequency change.

For SNG623, at the first location, the measured mean and standard deviation of G-band position was ~ 1581.9±0.4 cm^{-1} (at 21 °C), 1580.5 ±0.7 cm^{-1}(100 °C), 1575.4±0.4 cm^{-1} (350 °C), 1573.1±0.4 cm^{-1} (450 °C) and 1563.5±0.7 cm^{-1} (800 °C) respectively (Fig. 7a). At the second location, the measured mean and standard deviation of the G-band position was ~ 1581.9±1.4 cm^{-1} (21 °C), 1580.8±0.7 cm^{-1} (100 °C), 1575.4±0.7 cm^{-1} (350 °C), 1572.9±1.0 cm^{-1} (450 °C), and 1563.4±0.9 cm^{-1} (800 °C), as in Fig. 7b.

For T220 at the first location, the measured mean and standard deviation of the G-band position from each map was ~ 1582.1±0.4 cm^{-1}(at 21 °C), 1581.0±0.4 cm^{-1} (100 °C), 1575.6±0.4 cm^{-1} (350 °C), 1573.1±0.3 cm^{-1} (450 °C) and 1563.8±0.5 cm^{-1} (800 °C) (Fig. 7c). Data from the second location were 1582.7±0.7 cm^{-1} (21 °C), 1581.6 ±0.8 cm^{-1} (100 °C), 1576.1±0.7 cm^{-1} (350 °C), 1573.4±1.0 cm^{-1} (450 °C) and 1564.3±0.6 cm^{-1} (800 °C), respectively, as in Fig. 7d.

The linearity of the G-band shift averaged over the two regions was 0.023 ± 0.002 cm^{-1} °C^{-1} for SNG623 graphite and 0.024 ± 0.002 cm^{-1} °C^{-1} for T220 graphite. From these data and Fig. 7e, it is clear that the measured G-band standard deviation is consistent at each temperature and shows no definitive trend of any reduction with increasing temperature. The absolute Raman shift change caused by hydrostatic stress was previously calibrated on a piece of Gilsocarbon crystal that was free of pores; this gave a value of ~ 180 ± 5 MPa/cm^{-1} and this has been directly applied to these fine-grained graphite for quantifying the amount of residual stress relief [25]. The largest residual stress relaxation in SNG623 graphite was ~ 88–95 MPa estimated from the change in the standard deviation from 1.4 cm^{-1} at 21 °C to 0.9 cm^{-1} at 800 °C. This number for T220 graphite was ~ 17–19 MPa estimated from the change of 0.7 cm^{-1} at 21 °C to 0.6 cm^{-1} at 800 °C. For comparison, stresses at this level only account for up to 2–10% of the true strength (1000 MPa) obtained from micro-cantilever bending test of Gilsocarbon graphite specimens that are free of large porosity/defects [14].

The important message here is that both grades of fine-grained graphite exhibit limited residual stress relaxation at high temperatures up to 800 °C. Such relaxation of tensile residual stresses would contribute significantly to improved strength and toughness at elevated temperatures, as seen in Gilsocarbon [25]. However, in the fine grain graphites, there is only a small relaxation - nothing to the extent of that previously found for the coarser-grained Gilsocarbon - consistent with the current observations of much smaller improvements in elevated temperature strength and fracture toughness of the fine-grained graphites. Although the exact mechanistic correlation between nano-scale residual stress and bulk scale strength and toughness is not precisely

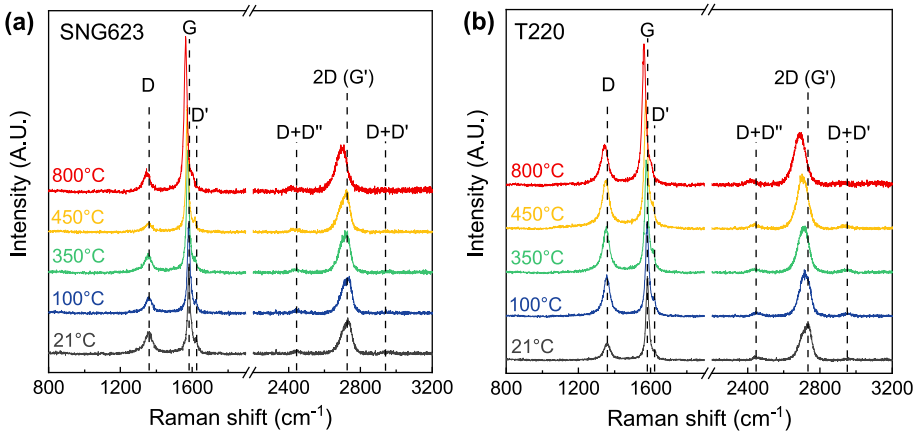

Fig. 6. Example Raman spectra of SNG623 and T220 nuclear graphite taken at elevated temepratrues from room temperature of 21°C to 800°C, showing the E_{2g} Raman mode-induced G-band and disorder-induced D- and D′-bands. Second-order Raman scattering can also be seen as a G′-band. A shift in band position is seen due to change in phonon frequency induced by high temperature. (a): SNG623 graphite and, (b): T220 graphite. Notations are quoted from Ref. [60].

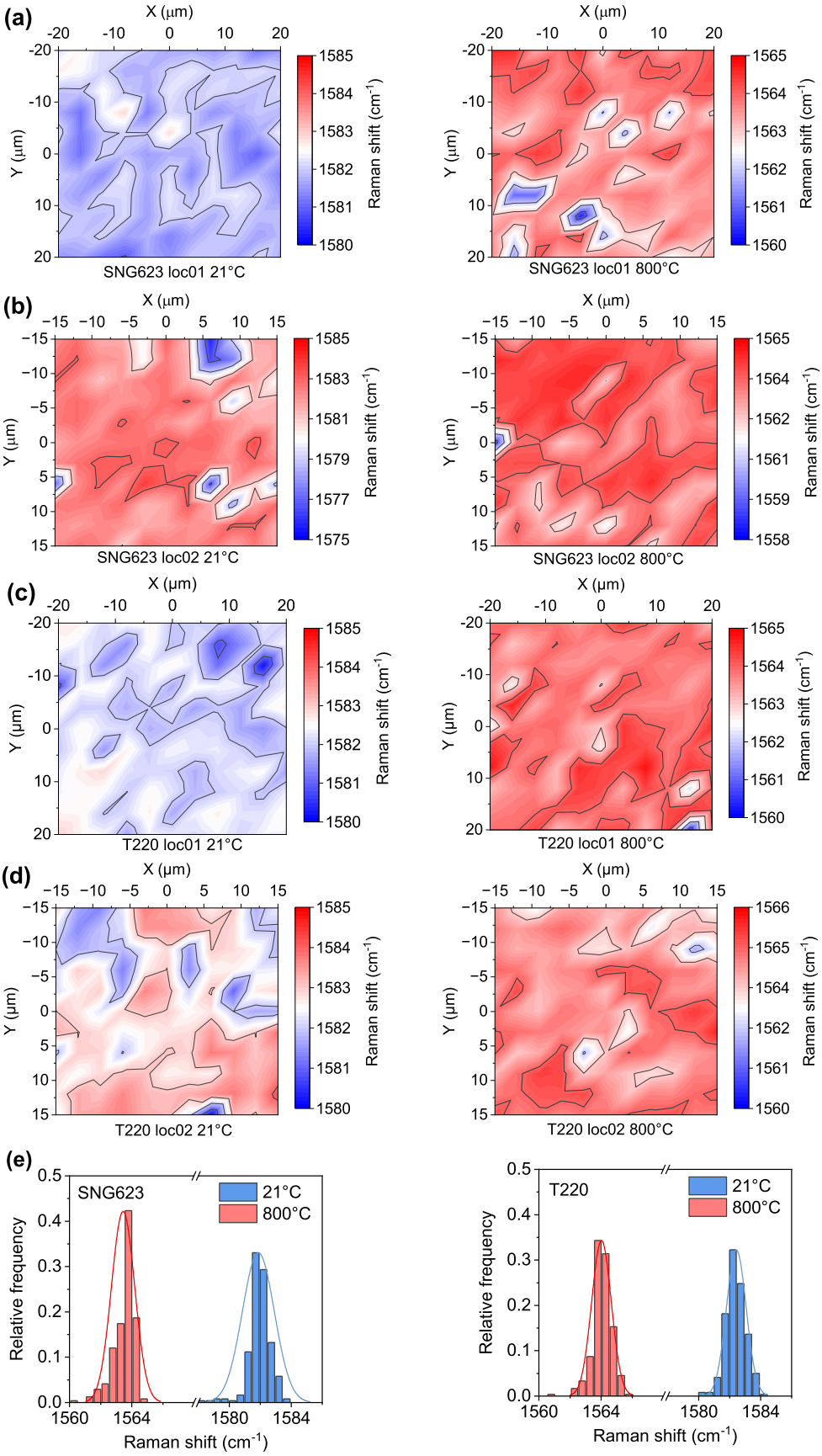

(caption on next page)

Fig. 7. High-temperature Raman mapping of SNG623 and T220 fine-grained graphite measured on their freshly fractured surfaces. These are G-band position maps for SNG623 and T220 graphite comparing 21 °C and 800 °C, showing no significant reduction in the variation of the G-band positions, in contrast to previous findings for Gilsocarbon graphite where the this distribution was distinctly narrowed [25]. (a): 1st mapping location of SNG623 graphite. (b): 2nd mapping location of SNG623 graphite. (c): 1st mapping location of T220 graphite and, (d): 2nd mapping location of T220 graphite. (e): Histograms of all the measured Raman G-band position for SNG623 and T220 graphite comparing 21 °C and 800 °C; no significant change in G-band position distribution profile can be seen with curves fitted to normal distributions. These indicate that there is no significant residual stress relaxation in these two fine-grained graphites at 800 °C.

known, this set of data act as further evidence (in addition to that in Gilsocarbon graphite [17]) for the correlation between magnitude of tensile stress relaxation and the degree of the increase in strength and toughness at higher temperatures.

4. Discussion

Before the detailed discussion of the results, it is worth noting that during the measurement of the crack lengths for fracture toughness calculations, a straight crack front was assumed with crack lengths being measured every 100 slice in the tomographic images for each specimen across out-of-plane thickness (B). There are advanced crack tip detection techniques in literature such as image edge detection algorithm based on both phase congruency [38,61] and wavelet modulus maxima [62] that allows crack tip and length to be identified from curved crack front. In fact the difference between stress intensity factors reported from straight crack assumption and curved crack in SNG742 graphite was only reported to be 3% [62]. Future work by incorporating these image detection techniques into crack tip identification in these fine-grained graphites at high temperature could be carried out to examine such differences and to compare the measured crack lengths between image segmentation and edge detection algorithm.

The use of numerical solution of JMAN for J-integral provides a robust method for determining local strain energy release rate without the need of accurately identifying crack tip location and therefore suitable for quasi-brittle porous material like nuclear graphite whose crack profile and propagation could potentially be complicated [56,63–65]. Calculated J values at the corresponding crack lengths as described in Results section showed good trend consistency with those experimentally derived from ASTM E1820 Standard. Mode I K_{IC} values back-calculated from both JMAN and ASTM standard are in a similar range with mode I fracture toughness reported by other researchers in various fine-grained graphite including IG-110, IG-430, NBG-25, SNG742 and T220 [2,30,35,36,38,66–68] using a range of specimen geometries and testing methods. This suggests that these modern fine-grained graphites must be considered as highly fracture-prone engineering materials. The local method using J-integral based on digital volume correlation analysis is particularly useful for the surveillance samples with non-standard geometries such as shorter beams in bending with shear stress component or thinner samples that cannot satisfy ASTM E1820 validity requirements.

The competition between intrinsic damage processes ahead of the crack tip and toughening mechanisms that operate extrinsically by shielding at, or in the wake of, the crack tip invariably act to dictate the fracture behaviour of quasi-brittle materials such as graphite [39,69]. Due to their brittle nature, intrinsic toughening mechanisms which primarily result from plasticity are limited in such materials, although inelastic deformation generated by the development of microcracking in the process zone ahead of the crack tip, as in graphite, can generate post elastic limit nonlinearity that resembles plasticity and can similarly serve to relieve local regions of high stress to elevate the crack-initiation toughness. Extrinsic toughening mechanisms, conversely, tend to shield the stresses and strains locally experienced by the crack tip, thereby providing for crack-growth toughness.

In Gilsocarbon graphite, the large filler particles and circular or lenticular pores play an important role in dictating a tortuous fracture path, which serves to promote rising R-curves, to enhance the (extrinsic) toughness and generate stable crack growth prior to final fracture [17,70,71]. However, in the fine-grained SNG623 and T220 graphites, the filler grains and pores are substantially smaller and, as such, provided an inconsequential contribution to deflecting the crack path to increase resistance to crack growth. Fractographic observations from tomographic images from all fractured specimens demonstrate that the main cracks propagated in a predominantly linear fashion with marginal tortuosity. Despite minor deflections and local bifurcations in the crack trajectory with limited crack bridging, the degree of extensive toughening in these fine-grained materials appears to be minimal, with the result that there was only a limited R-curve following crack initiation at both ambient and high temperatures, indicative of very little stable crack extension prior to final fracture. In short, both the fine-grained graphites display far more brittle behaviour from the lack of a significant R-curve than the coarser-grained Gilsocarbon graphite.

In a similar vein, there was little evidence of microcracking observed in the fine-grained graphites at both ambient and high temperatures in the three point bending configuration adopted in present study, in contrast to Gilsocarbon where the degree of microcracking was extensive [25]. Microcracking is a form of inelasticity in that it generates nonlinear constitutive behaviour in graphite and can relieve regions of high stress akin to plastic deformation; the absence of such marked inelasticity in the SNG623 and T220 graphites is further confirmed by the linear tensile strain increase with increasing distance away from the neutral plane in the unnotched beam specimens. In terms of the exact failure stresses/strains, SNG623 has a higher flexural strength and failure strain than T220 at all temperatures tested as evident by the DVC analysis. Further, the high temperature tensile failure strains are lower than room temperature for both materials, which implies that there is a significant increase in the modulus of these graphites with increase in temperature. Indeed, it has been known since Green's measurements in 1951 [57,72] that the strength and modulus increase with temperature in nuclear graphite materials. The current results suggest that the modulus is increasing at faster rate than the strength to possibly result in the decrease in failure strains at 1100 °C, i.e., these fine-grained graphite materials become more brittle at 1100 °C. It is unclear in terms of the underlying mechanisms as to what is leading to a different rate of increase in modulus and strength and their increase rates. To further confirm this phenomenon, it is suggested that longer beam specimens to be tested under bending and/or uniaxial tension/compression using ASTM standard geometry to derive failure stress/strain and modulus based on ASTM standard analytical models over a range of temperatures. It is best to test many more samples at each condition using Weibull type statistical analysis to obtain the average values as well as scatter in the data. Note the absence of microcracking and lower high-temperature failure strains observed in present work are indeed consistent with the more brittle-like behaviour of the fine-grained graphites compared to the coarser-grained Gilsocarbon of the same specimen geometry and tested by the same methodology [25].

It is generally recognised that graphite crystal thermal expansion at high temperature can contribute to the closure of nanoscale Mrozowski type porosity [25,59,73,74]. Marrow et al. [59,75] and Liu et al. [25,59,75] have previously found, using neutron diffraction combined with digital image correlation, that the crystals in Gilsocarbon graphite were able to accommodate more tensile strains at temperatures higher than 600 °C, which was attributed to the closure of thermal shrinkage microcracks and the concomitant effect of tensile residual stress relaxation at the nano-scale. Both of these phenomena are consistent with the marked progressive increase in fracture toughness (for both crack

initiation and growth) in Gilsocarbon with increasing temperature between ambient and 1000 °C. However, in fine-grained graphites, the amount of residual stresses relaxed at elevated temperatures are significantly smaller and thus this potent mechanism of the relaxation of the tensile residual stresses which acts to increase the toughness at high temperature is simply far less of a factor. The exact correlation between the evolution of a large population of nanoscale porosity to the relaxation of tensile residual stress over large length-scales (tens of micrometre to millimetre), and to bulk mechanical properties at high temperature is yet to be established, predominantly due to the limitation in the resolution and probe volume of characterisation techniques and quite often a compromise must be made. This is certainly a very challenging topic and requires substantial amount of future work to investigate.

The fracture of quasi-brittle nuclear graphite is closely related to the development and propagation of fracture process zone (FPZ) ahead of a main crack tip. FPZ is considered to be a region containing extensive amount of microcracking that consumes elastic strain energy, leading to local non-linearity and contributing to energy-based *R*-curve that is sensitive to specimen geometry (and different stress states due to different loading conditions). From the summative comparison by Becker et al. [63], it has been found that the size of FPZ is different in Gilsocarbon graphite tested by double torsion, compact tension and 3-point bending, with the largest FPZ of 8–10 mm being found in double torsion technique accompanied with a highest and steepest rising *R*-curve. Whereas the 3-point bending configuration had the smallest FPZ of 2–3 mm and lowest *R*-curve and was therefore considered to be applicable to linear elastic fracture mechanics (LEFM) assessment which further supports the use of linear elastic material model and strain-stress relationship in JMAN code in this work. In current study of SNG623 and T220 graphite and the previous work on Gilsocarbon graphite [25], the exact same specimen geometry and testing methodology have been employed to rule out the effect of testing configuration. Future work of characterising the exact FPZ sizes in fine-grained graphite is still needed to better understand the development and propagation of FPZ and its size effect [63,76] via a consistent testing configuration over a range of temperatures.

The FPZ in fine-grained graphite has been experimentally measured by Chen et al. [77] and Tang et al. [78,79] suggesting that, in general, the stable crack propagation stage of nuclear graphite is relatively short compared to other coarse-grained quasi-brittle materials. As shown in present work, this phenomenon is more severe for fine-grained graphite. However, such lack of stable crack propagation stage in SNG623 and T220 was only observed by comparing with Gilsocarbon graphite using the same single-edge notch bend (SENB) fracture toughness testing geometry in this work, it would be beneficial to conduct fracture toughness experiments with different specimen geometries under different loading configurations to further substantiate such statement especially at elevated temperatures.

The fracture toughness values and toughening mechanisms observed are comparable to those reported in literature. Example from IG-11 graphite [80] showed critical stress intensity factor at crack initiation of only 0.74 MPa$\sqrt{m}$ for all a_0/W ratio < 0.6 in compact tension specimen, although they reported a significant contribution from grain bridging at the wake of the main crack to the measured initial sharp increase in K_R-curve of IG-11 graphite. Microcracking events in the frontal fracture process zone have also been identified. Evidently, despite the presence of grain-bridging and filler pullout toughening mechanisms in fine-grained graphite, their contribution towards crack initiation resistance is limited, seen as the lower value [80,81] than that of conventional coarser-grained graphite such as Gilsocabon graphite with a crack initiation resistance of $\sim$ 1.2–1.5 MPa$\sqrt{m}$ being reported [25,67,82]. The higher crack initiation resistance in Gilsocarbon graphite was attributed to increased difficulty of microcrack initiation and coincidental alignment among microcracks to form macrocracks due to the presence of spherical fillers [67]. In Fazluddin's work [67] where a systematic comparison of the *R*-curve behaviour obtained by both 3-point bending and compact tension tests of Gilsocarbon graphite and IG-110 graphite was conducted, IG-110 graphite was found to consistently exhibit lower stress intensity based K_R-curve than Gilsocarbon graphite, with a typical crack initiation toughness of 0.8–0.9 MPa$\sqrt{m}$. These indicate that fine-grained graphite exemplified by IG-11 (0) can be less resistant to crack initiation.

With regard to crack growth resistance, a higher K_R-curve might not always indicate significant resistance to crack propagation in relation to the energy dissipated during the fracture process and this is exemplified by the higher K_{IC} but lower *J-R* curve for Gilsocarbon graphite compared to PGA graphite [82]. The significantly increased work of fracture and *J-R* curve in PGA graphite was attributed to the more significant crack bridging and crack branching, indicative of the greater extent of energy dissipation via irreversible deformation processes through the cracking of the coarser micro-texture of PGA graphite [83]. A lower value of K_{IC} in PGA graphite was simply attributed to its lower material strength [82]. Similarly, from the fractographic examination of IG-110 and Gilsocarbon graphite by Fazluddin [67], smaller filler grains in IG-110 graphite are easier for crack to propagate through which could further be promoted by the weakest link at filler-binder interface such as porosity, making the overall crack deflection less pronounced. Gilsocarbon graphite, on the contrary, displayed more intricate crack profile and crack-filer/crack-binder interactions due to the presence of randomly distributed larger spherical filler grains, with such crack path being further complicated by its interaction with porosity generating secondary cracks.

The crack growth resistance and *R*-curve behaviours of fine grain graphite can also be compared to Gilsocarbon graphite by normalising crack extension Δa within ASTM E1820 standard specification to uncracked ligament b_0, i.e., $\Delta a/b_0$. Previous study on Gilsocarbon graphite [25] demonstrated increasingly rising *R*-curves for all $\Delta a/b_0 <$ 0.42 (maximum valid Δa $\sim$1 mm). Whereas the stable crack growth *J-R*-curves stopped at a largest $\Delta a/b_0 = 0.15$ (maximum valid Δa $\sim$0.32 mm) for SNG623 and a largest $\Delta a/b_0 = 0.25$ (maximum valid Δa $\sim$0.57 mm) for T220 even at 1100 °C in this work. Such comparison can also be made to the Gilsocarbon graphite data from Fazluddin [67] in which rising *R*-curves have been observed for $\Delta a/b_0 < 0.5$; and similarly from Ouagne et al. [82] where rising R-curves were seen for all $\Delta a/b_0 < 0.25$ (up to Δa $\sim$10 mm) and did not start falling until $\Delta a/b_0 = 0.6$ in Gilsocarbon grapihte. This is consistent with the observation in present work that these two fine-grained graphite suffered from unstable crack growth at an earlier stage of fracture even at elevated temperatures.

More fracture studies of coarser-grained and fine-grained graphite can be found in literature including H-451, PGA and Gilsocarbon graphite [18,63,67,70,76,82–87], NBG-10, NBG-18 and NBG-17 graphite [7,56,63,88–90], IG-11(0) [2,30,35,67,80,81,91], IG-430 [2,35], SNG742 and T220 [36,38]. Although fracture behaviour and fracture toughness of fine-grained graphite have been studied by many, with typical mode I fracture toughness for various grades of medium-fine and fine-grained graphite being reported to be in a range of about 0.8–1.5 MPa$\sqrt{m}$ [2,7,36,38,66,67,88] depending on test configuration, very limited open literature studied the failure and fracture process/mechanisms at high temperatures with even less data on their high-temperature *R*-curve behaviours[6]. The limited available open literatures of un-irradiated nuclear graphite high temperature fracture behaviour are mostly focussed on coarser-grained graphite [25,59,75,87]. To this end, a direct comparison and correlation of SNG623 and T220 graphite data to those from better-documented fine-grained graphites at high temperature is not readily feasible, and it is certainly part of future work to establish a relatively complete high temperature fracture dataset, spanning from existing coarser-grained historic grades to fine-grained grades.

5. Conclusion

To conclude, we conducted *in situ* high temperature mechanical

testing of two modern fine-grained graphite materials to investigate their strength, fracture properties and damage tolerance, with 4D imaging using synchrotron X-ray computed micro-tomography, high-resolution 3D strain analysis by digital volume correlation and residual stress evaluation by high-temperature micro-Raman mapping. Results demonstrate that fine-grained graphite materials, exemplified by SNG623 and T220, are less fracture-resistant compared to conventional coarser-grained Gilsocarbon graphite. There is far lower elevation in strength and fracture toughness at elevated temperatures in these fine-grained graphite materials with a reduced tensile failure strain at 1100 °C. Moreover, they had a shorter stable crack extension stage prior to final failure which is characteristic of the conventional coarser-grained graphites such as Gilsocarbon graphite. The increase in elastic modulus with the increase in temperature is much faster than the increase in strength with temperature, which resulted in reduced failure strain at 1100 °C. These findings must be considered when modelling the performance of fine-grained graphite materials in nuclear applications of advanced fission systems and Gen IV reactors as well as next generation multi-megawatt (MW)-class proton accelerator facilities, where the operation temperature will be pushed well-beyond 700 °C [92,93].

Data availability

The data that support the findings of this study are available from the corresponding author, Dong Liu, at Dong.liu@bristol.ac.uk and dong.liu@eng.ox.ac.uk, upon reasonable request.

CRediT authorship contribution statement

Ming Jiang: conducted the analysis of X-ray tomography datasets in terms of image segmentation and digital volume correlation, crack length measurements and JMAN code J-integral analysis; conducted Raman spectroscopy measurements and related data analysis. produced most of the figures and wrote the first draft and contributed to the editing of the paper. **Jon Ell and Harold Barnard:** assisted the experiments. **Houzheng Wu:** provided the materials, discussion of results and manuscript editing. **Martin Kuball:** provided access to the Raman facility, discussion of the results and manuscript editing. **Robert O. Ritchie:** Supervision of Jon Ell, discussion of results and manuscript editing. **Dong Liu:** designed and conducted the in situ high temperature X-ray tomography experiments, reconstructed the data, conducted the R-curve analysis, supervised the work, secured funding and resources and contributed to the writing and edits of the manuscript.

Declaration of competing interest

The authors declare that they have no known competing financial interests or personal relationships that could have appeared to influence the work reported in this paper.

Acknowledgments

The research was primarily supported by the UK Engineering and Physical Sciences Research Council (EP/N004493/2, EP/T000368/1). The authors acknowledge the use of beamline 8.3.2 at the Advanced Light Source, Lawrence Berkeley National Laboratory, USA, which is supported by the Office of Science of the U.S. Department of Energy under Contract No. DE-AC02-05CH11231. D.L. and M.J. would like to thank Prof. Mahmoud Mostafavi for providing access to the JMAN code developed by his group.

Appendix A. Supplementary data

Supplementary data to this article can be found online at https://doi.org/10.1016/j.carbon.2024.118924.

References

[1] T. Abram, S. Ion, Generation-IV nuclear power: a review of the state of the science, Energy Pol. 36 (2008) 4323–4330.
[2] T. Yamada, et al., Evaluation of fracture toughness of fine-grained isotropic graphites for HTGR, Nucl. Eng. Des. 271 (2014) 323–326.
[3] B. Marsden, A. Jones, G. Hall, M. Treifi, P. Mummery, in: Structural Materials for Generation IV Nuclear Reactors, Elsevier, 2017, pp. 495–532.
[4] US Department of Energy, W., DC, A Technology Road-Map for Generation-IV Nuclear Energy Systems, Generation-IV International Forum, 2002.
[5] D.A. Petti, The Next Generation Nuclear Plant, Idaho National Lab.(INL), Idaho Falls, ID (United States), 2009.
[6] Jordan, M. S., Liu, D., Jiang, M. & Tzelepi, A. in Symposium on Graphite Testing for Nuclear Applications: the Validity and Extension of Test Methods for Material Exposed to Operating Reactor Environments. 80-129 (ASTM International).
[7] G. Liu, et al., An investigation of fracture behaviors of NBG-18 nuclear graphite using in situ mechanical testing coupled with micro-CT, J. Mater. Res. (2023) 1–10.
[8] L. Lommers, G. Honma, NGNP High Temperature Materials White Paper, Idaho National Lab.(INL), Idaho Falls, ID (United States), 2012.
[9] P. Kasten, et al., Graphite behavior and its effects on MSBR performance, Nucl. Eng. Des. 9 (1969) 157–195.
[10] N. Simos, et al., 120 GeV neutrino physics graphite target damage assessment using electron microscopy and high-energy x-ray diffraction, Physical Review Accelerators and Beams 22 (2019), https://doi.org/10.1103/PhysRevAccelBeams.22.041001.
[11] N. Simos, et al., Proton irradiated graphite grades for a long baseline neutrino facility experiment, Physical Review Accelerators and Beams 20 (2017), https://doi.org/10.1103/PhysRevAccelBeams.20.071002.
[12] N. Simos, et al., Irradiation damage studies of high power accelerator materials, J. Nucl. Mater. 377 (2008) 41–51, https://doi.org/10.1016/j.jnucmat.2008.02.074.
[13] D. Liu, et al., Towards understanding the influence of porosity on mechanical and fracture behaviour of quasi-brittle materials: experiments and modelling, Int. J. Fract. 205 (2017) 57–72, https://doi.org/10.1007/s10704-017-0181-7.
[14] D. Liu, K. Mingard, O.T. Lord, P. Flewitt, On the damage and fracture of nuclear graphite at multiple length-scales, J. Nucl. Mater. 493 (2017) 246–254, https://doi.org/10.1016/j.jnucmat.2017.06.021.
[15] D. Liu, P.J. Heard, S. Nakhodchi, P.E.J. Flewitt, in: *Graphite Testing for Nuclear Applications: the Significance of Test Specimen Volume and Geometry and the Statistical Significance of Test Specimen Population* Ch. Stp157820130127, 2014, pp. 84–104.
[16] C.N. Morrison, Lattice-Modelling of Nuclear Graphite for Improved Understanding of Fracture Processes, The University of Manchester, United Kingdom, 2016.
[17] R. Moskovic, P.J. Heard, P.E. Flewitt, M. Wootton, Overview of strength, crack propagation and fracture of nuclear reactor moderator graphite, Nucl. Eng. Des. 263 (2013) 431–442.
[18] A. Hodgkins, T.J. Marrow, M.R. Wootton, R. Moskovic, P.E.J. Flewitt, Fracture behaviour of radiolytically oxidised reactor core graphites: a view, Mater. Sci. Technol. 26 (2013) 899–907, https://doi.org/10.1179/026708309x12526555493477.
[19] B. Šavija, et al., Experimentally informed multi-scale modelling of mechanical properties of quasi-brittle nuclear graphite, Eng. Fract. Mech. 153 (2016) 360–377, https://doi.org/10.1016/j.engfracmech.2015.10.043.
[20] T.D. Burchell, T.R. Pavlov, in: Rudy J.M. Konings, Roger E. Stoller (Eds.), Comprehensive Nuclear Materials, second ed., Elsevier, 2020, pp. 355–381.
[21] T. Marrow, et al., In situ measurement of the strains within a mechanically loaded polygranular graphite, Carbon 96 (2016) 285–302.
[22] M. Jiang, et al., Multiple length-scale microstructural characterisation of four grades of fine-grained graphite, J. Nucl. Mater. 550 (2021) 152876.
[23] J.D. Arregui-Mena, et al., Multiscale characterization and comparison of historical and modern nuclear graphite grades, Mater. Char. (2022) 112047.
[24] D. Liu, et al., A macro-scale ruck and tuck mechanism for deformation in ion-irradiated polycrystalline graphite, Carbon 173 (2021) 215–231.
[25] D. Liu, B. Gludovatz, H.S. Barnard, M. Kuball, R.O. Ritchie, Damage tolerance of nuclear graphite at elevated temperatures, Nat. Commun. 8 (2017) 15942, https://doi.org/10.1038/ncomms15942.
[26] M.S.L. Jordan, *Studies of the Crack Initiation and Notch Sensitivity Behaviour of Gilsocarbon* Doctor of Philosophy Thesis, University of Oxford, 2019.
[27] R. Moskovic, et al., Understanding fracture behaviour of PGA reactor core graphite: perspective, Mater. Sci. Technol. 30 (2013) 129–145, https://doi.org/10.1179/1743284713y.0000000354.
[28] C. Karthik, J. Kane, D.P. Butt, W.E. Windes, R. Ubic, Microstructural characterization of next generation nuclear graphites, Microsc. Microanal. 18 (2012) 272–278.
[29] T.D. Burchell, T.R. Pavlov, Graphite: Properties and Characteristics, 2020.
[30] A.A. Campbell, A.A. Wereszczak, M.A. Snead, Y. Katoh, Understanding the effect of specimen size on the properties of fine-grain isotropic nuclear graphite for irradiation studies: mechanical properties, J. Nucl. Mater. (2023) 154263.
[31] M. Mostafavi, S.A. McDonald, H. Çetinel, P.M. Mummery, T.J. Marrow, Flexural strength and defect behaviour of polygranular graphite under different states of stress, Carbon 59 (2013) 325–336, https://doi.org/10.1016/j.carbon.2013.03.025.
[32] B. Šavija, et al., Modelling deformation and fracture of Gilsocarbon graphite subject to service environments, J. Nucl. Mater. 499 (2018) 18–28, https://doi.org/10.1016/j.jnucmat.2017.10.076.
[33] H. McCoy, et al., New developments in materials for molten-salt reactors, Nucl. Appl. Technol. 8 (1970) 156–169.

[34] B.J. Marsden, G.N. Hall, Graphite in gas-cooled reactors, Reference Module in Materials Science and Materials Engineering 14 (2020) 357–421.
[35] S.-H. Chi, Comparison of fracture toughness (KIc) and strain energy release rate (G) of selected nuclear graphites, J. Nucl. Mater. 476 (2016) 188–197.
[36] Y. Gao, D.K. Tsang, Investigation on failure assessment method for nuclear graphite components, Nucl. Eng. Technol. 52 (2020) 206–210.
[37] M.C. Carroll, Initial Comparison of Baseline Physical and Mechanical Properties for the VHTR Candidate Graphite Grades, Idaho National Lab.(INL), Idaho Falls, ID (United States), 2014.
[38] X. Jin, et al., Crack propagation in fine grained graphites under mode I and mixed-mode loading, as observed in situ by microtomography, Carbon 193 (2022) 356–367.
[39] R.O. Ritchie, D. Liu, Introduction to Fracture Mechanics, Elsevier, 2021.
[40] J.P. Forna-Kreutzer, et al., Full-field characterisation of oxide-oxide ceramic-matrix composites using X-ray computed micro-tomography and digital volume correlation under load at high temperatures, Mater. Des. 208 (2021) 109899.
[41] G. Yuan, et al., In situ high-temperature 3D imaging of the damage evolution in a SiC nuclear fuel cladding material, Mater. Des. 227 (2023) 111784.
[42] B. Marz, et al., Data related to the mesoscopic structure of iso-graphite for nuclear applications, Data Brief 19 (2018) 651–659, https://doi.org/10.1016/j.dib.2018.05.003.
[43] D02.F0, C. (ASTM International, West Conshohocken, PA, 2019.
[44] Q. Huang, H. Tang, Porosity analysis of superfine-grain graphite IG-110 and ultrafine-grain graphite T220, Mater. Sci. Technol. 35 (2019) 962–968.
[45] A. Haboub, et al., Tensile testing of materials at high temperatures above 1700 C with in situ synchrotron X-ray micro-tomography, Rev. Sci. Instrum. 85 (2014) 083702.
[46] H.A. Bale, et al., Real-time quantitative imaging of failure events in materials under load at temperatures above 1,600 C, Nat. Mater. 12 (2013) 40–46.
[47] T.J. Pirzada, et al., In situ observation of the deformation and fracture of an alumina-alumina ceramic-matrix composite at elevated temperature using x-ray computed tomography, J. Eur. Ceram. Soc. 41 (2021) 4217–4230.
[48] D. Liu, et al., X-ray tomography study on the crushing strength and irradiation behaviour of dedicated tristructural isotropic nuclear fuel particles at 1000° C, Mater. Des. 187 (2020) 108382.
[49] M. Dierick, B. Masschaele, L. Van Hoorebeke, Octopus, a fast and user-friendly tomographic reconstruction package developed in LabView, Meas. Sci. Technol. 15 (2004) 1366.
[50] B. März, K. Jolley, R. Smith, H. Wu, Near-surface structure and residual stress in as-machined synthetic graphite, Mater. Des. 159 (2018) 103–116, https://doi.org/10.1016/j.matdes.2018.08.041.
[51] M. Kuball, Raman spectroscopy of GaN, AlGaN and AlN for process and growth monitoring/control, Surf. Interface Anal.: An International Journal devoted to the development and application of techniques for the analysis of surfaces, interfaces and thin films 31 (2001) 987–999.
[52] J. Schindelin, et al., Fiji: an open-source platform for biological-image analysis, Nat. Methods 9 (2012) 676–682.
[53] C.A. Schneider, W.S. Rasband, K.W. Eliceiri, NIH Image to ImageJ: 25 years of image analysis, Nat. Methods 9 (2012) 671–675.
[54] M. Mostafavi, et al., Three-dimensional crack observation, quantification and simulation in a quasi-brittle material, Acta Mater. 61 (2013) 6276–6289, https://doi.org/10.1016/j.actamat.2013.07.011.
[55] K. Madi, et al., Computation of full-field displacements in a scaffold implant using digital volume correlation and finite element analysis, Med. Eng. Phys. 35 (2013) 1298–1312.
[56] T. Becker, M. Mostafavi, R. Tait, T. Marrow, An approach to calculate the J-integral by digital image correlation displacement field measurement, Fatig. Fract. Eng. Mater. Struct. 35 (2012) 971–984.
[57] T. Maruyama, M. Eto, T. Oku, Elastic modulus and bend strength of a nuclear graphite at high temperature, Carbon 25 (1987) 723–726.
[58] Committee, E. (ASTM International, West Conshohocken, PA, 2017.
[59] D. Liu, et al., In situ measurement of elastic and total strains during ambient and high temperature deformation of a polygranular graphite, Carbon 163 (2020) 308–323, https://doi.org/10.1016/j.carbon.2020.03.020.
[60] A.C. Ferrari, D.M. Basko, Raman spectroscopy as a versatile tool for studying the properties of graphene, Nat. Nanotechnol. 8 (2013) 235–246, https://doi.org/10.1038/nnano.2013.46.
[61] X. Jin, et al., Assessment of the fracture toughness of neutron-irradiated nuclear graphite by 3D analysis of the crack displacement field, Carbon 171 (2021) 882–893.
[62] J. Shen, et al., Combined evaluation of Young modulus and fracture toughness in small specimens of fine grained nuclear graphite using 3D image analysis, J. Nucl. Mater. 563 (2022) 153642.
[63] T. Becker, T. Marrow, R. Tait, Damage, crack growth and fracture characteristics of nuclear grade graphite using the Double Torsion technique, J. Nucl. Mater. 414 (2011) 32–43.
[64] S. Barhli, M. Mostafavi, A. Cinar, D. Hollis, T. Marrow, J-integral calculation by finite element processing of measured full-field surface displacements, Exp. Mech. 57 (2017) 997–1009.
[65] M. Mostafavi, T. Marrow, Quantitative in situ study of short crack propagation in polygranular graphite by digital image correlation, Fatig. Fract. Eng. Mater. Struct. 35 (2012) 695–707.
[66] G.R. Romanoski, T. Burchell, The Effects of Specimen Geometry and Size on the Fracture Toughness of Nuclear Graphites, Oak Ridge National Lab., TN (United States), 1991.
[67] S. Fazluddin, *Crack growth Resistance in Nuclear Graphite* Doctor of Philosophy Thesis, University of Leeds, 2002.
[68] T. Burchell, et al., The Fracture Toughness of Nuclear Graphite Grades, Revision 1, Oak Ridge National Lab.(ORNL), Oak Ridge, TN (United States), 2022.
[69] R.O. Ritchie, The conflicts between strength and toughness, Nat. Mater. 10 (2011) 817–822.
[70] J. Wade-Zhu, et al., 4D synchrotron X-ray microtomography of fracture in nuclear graphite after neutron irradiation and radiolytic oxidation, Carbon 168 (2020) 230–244.
[71] S.M. Barhli, et al., Synchrotron X-ray characterization of crack strain fields in polygranular graphite, Carbon 124 (2017) 357–371, https://doi.org/10.1016/j.carbon.2017.08.075.
[72] C. Malmstrom, R. Keen, L. Green, Some mechanical properties of graphite at elevated temperatures, J. Appl. Phys. 22 (1951) 593–600, https://doi.org/10.1063/1.1700013.
[73] A. Sutton, V. Howard, The role of porosity in the accommodation of thermal expansion in graphite, J. Nucl. Mater. 7 (1962) 58–71.
[74] G. Hall, B.J. Marsden, S.L. Fok, The microstructural modelling of nuclear grade graphite, J. Nucl. Mater. 353 (2006) 12–18, https://doi.org/10.1016/j.jnucmat.2006.02.082.
[75] T.J. Marrow, et al., In situ measurement of the strains within a mechanically loaded polygranular graphite, Carbon 96 (2016) 285–302, https://doi.org/10.1016/j.carbon.2015.09.058.
[76] M. Mostafavi, S. McDonald, P. Mummery, T. Marrow, Observation and quantification of three-dimensional crack propagation in poly-granular graphite, Eng. Fract. Mech. 110 (2013) 410–420.
[77] H.H.N. Chen, R.K.L. Su, S.L. Fok, H.G. Zhang, Fracture behavior of nuclear graphite under three-point bending tests, Eng. Fract. Mech. 186 (2017) 143–157, https://doi.org/10.1016/j.engfracmech.2017.09.030.
[78] Y. Tang, H. Chen, Characterization on crack propagation of nuclear graphite under three-point bending, Nuclear Materials and Energy 20 (2019) 100687, https://doi.org/10.1016/j.nme.2019.100687.
[79] Y.X. Tang, R.K.L. Su, H.N. Chen, Characterization on tensile behaviors of fracture process zone of nuclear graphite using a hybrid numerical and experimental approach, Carbon 155 (2019) 531–544, https://doi.org/10.1016/j.carbon.2019.08.081.
[80] M. Sakai, J.-I. Yoshimura, Y. Goto, M. Inagaki, R-curve behavior of a polycrystalline graphite: microcracking and grain bridging in the wake region, J. Am. Ceram. Soc. 71 (1988) 609–616, https://doi.org/10.1111/j.1151-2916.1988.tb06377.x.
[81] D. Kim, S.J. Oh, C. Jang, I.S. Kim, S.-H. Chi, Fracture toughness and crack growth resistance of the fine grain isotropic graphite, Carbon Sci 7 (2006) 19–26.
[82] O. Pierre, B.N. Gareth, M. Brian, Crack growth resistance in nuclear graphites, J. Phys. Appl. Phys. 35 (2002) 927, https://doi.org/10.1088/0022-3727/35/9/315.
[83] R. Moskovic, et al., Understanding fracture behaviour of PGA reactor core graphite: perspective, Mater. Sci. Technol. 30 (2014) 129–145.
[84] G.B. Neighbour, Microstructural Processes Leading to Fracture in Nuclear Graphites, University of Bath, United Kingdom, 1993.
[85] T. Wigger, B. Lin, C. Lupton, J. Marrow, J. Tong, A 3D full-field study of cracks in a nuclear graphite under mode I and mode II cyclic dwell loading conditions, Fatig. Fract. Eng. Mater. Struct. 43 (2020) 1646–1657.
[86] J. Marrow, et al., 3D studies of damage by combined X-ray tomography and digital volume correlation, Procedia materials science 3 (2014) 1554–1559.
[87] S. Sato, H. Awaji, H. Akuzawa, Fracture toughness of reactor graphite at high temperature, Carbon 16 (1978) 95–102, https://doi.org/10.1016/0008-6223(78)90004-0.
[88] P. Béghein, G. Berlioux, B. du Mesnildot, F. Hiltmann, M. Melin, NBG-17–An improved graphite grade for HTRs and VHTRs, Nucl. Eng. Des. 251 (2012) 146–149.
[89] E.-S. Kim, S.-D. Hong, Y.-W. Kim, Fracture behavior of nuclear grade graphite under mixed mode I-II, J. Ceram. Process. Res. 14 (2013) 251–254.
[90] H. Li, J. Li, G. Singh, A. Fok, Fracture behavior of nuclear graphite NBG-18, Carbon 60 (2013) 46–56, https://doi.org/10.1016/j.carbon.2013.03.055.
[91] D.-J. Kim, S.-J. Oh, C.-H. Jang, I.-S. Kim, S.-H. Chi, Fracture toughness and crack growth resistance of the fine grain isotropic graphite, Carbon letters 7 (2006) 19–26.
[92] K. Abe, et al., The T2K experiment, Nucl. Instrum. Methods Phys. Res. Sect. A Accel. Spectrom. Detect. Assoc. Equip. 659 (2011) 106–135, https://doi.org/10.1016/j.nima.2011.06.067.
[93] B. Densham, et al., in: 46th ICFA Advanced Beam Dynamics Workshop on High-Intensity and High-Brightness Hadron Beam, Morschach, Switzerland, October 2010.